Appendix B

Supplementary Information for Chapter 3: Experimental consequences of dynamic ion solvation

This appendix contains the supporting information for Chapter 3, and is analogous to the supporting information to the following manuscript:

Ieritano, C., Rickert, D., Featherstone, J., Honek, J. F., Campbell, J. L., Le Blanc, J. C. Y., Schneider, B. B., Hopkins, W. S. The Charge-State and Structural Stability of Peptides Conferred by Microsolvating Environments in Differential Mobility Spectrometry. *J. Am. Soc. Mass Spectrom.* **2021**. 32 (*4*), 956 – 968. ***Cover Article.***

https://pubs.acs.org/doi/abs/10.1021/jasms.0c00469

Table of Contents

Supporting figures and tables for Chapter 3

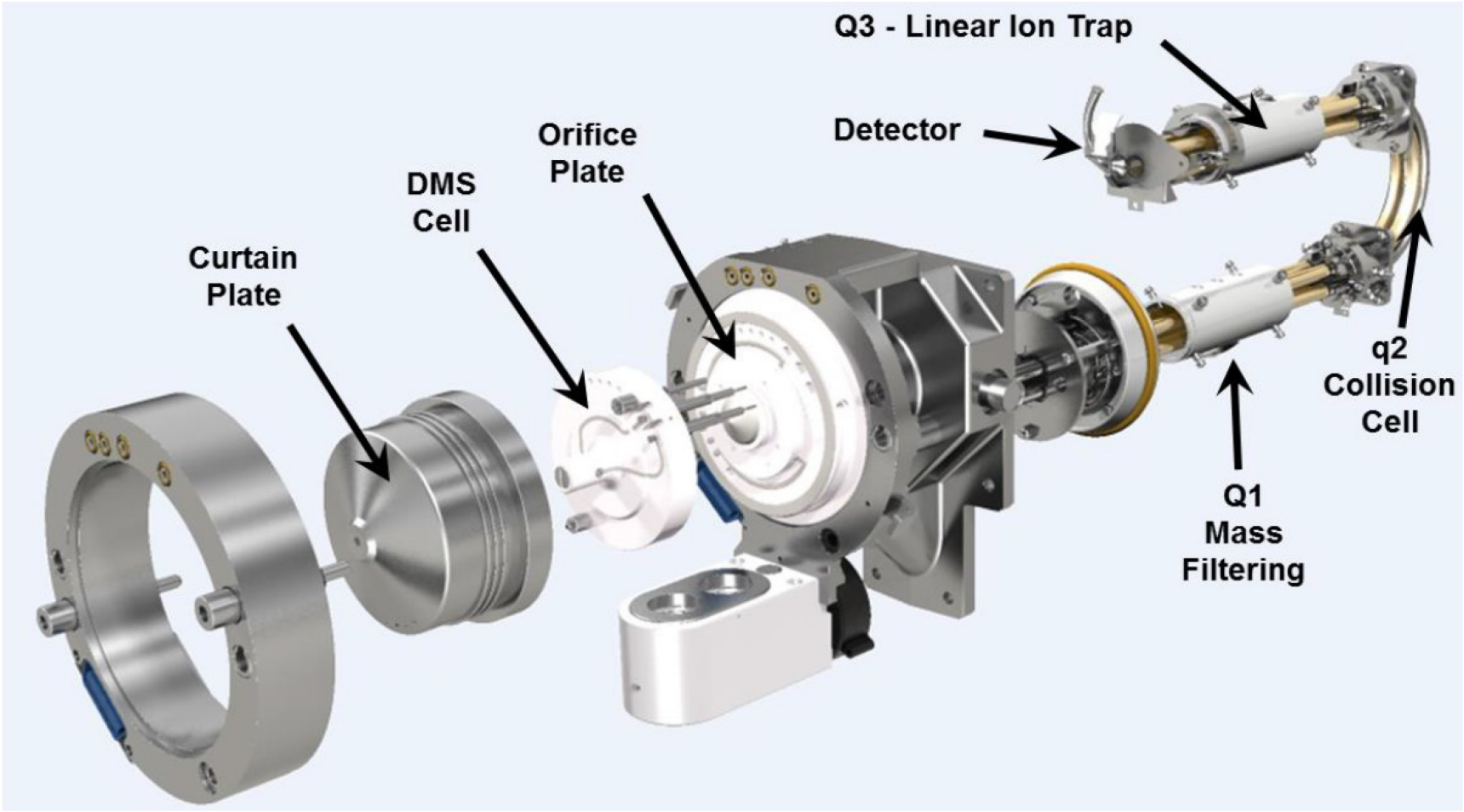

Figure S3-1. Schematic of the SELEXION system coupled to the 5500 QTRAP (SCIEX) hybrid triple-quadrupole mass spectrometer.

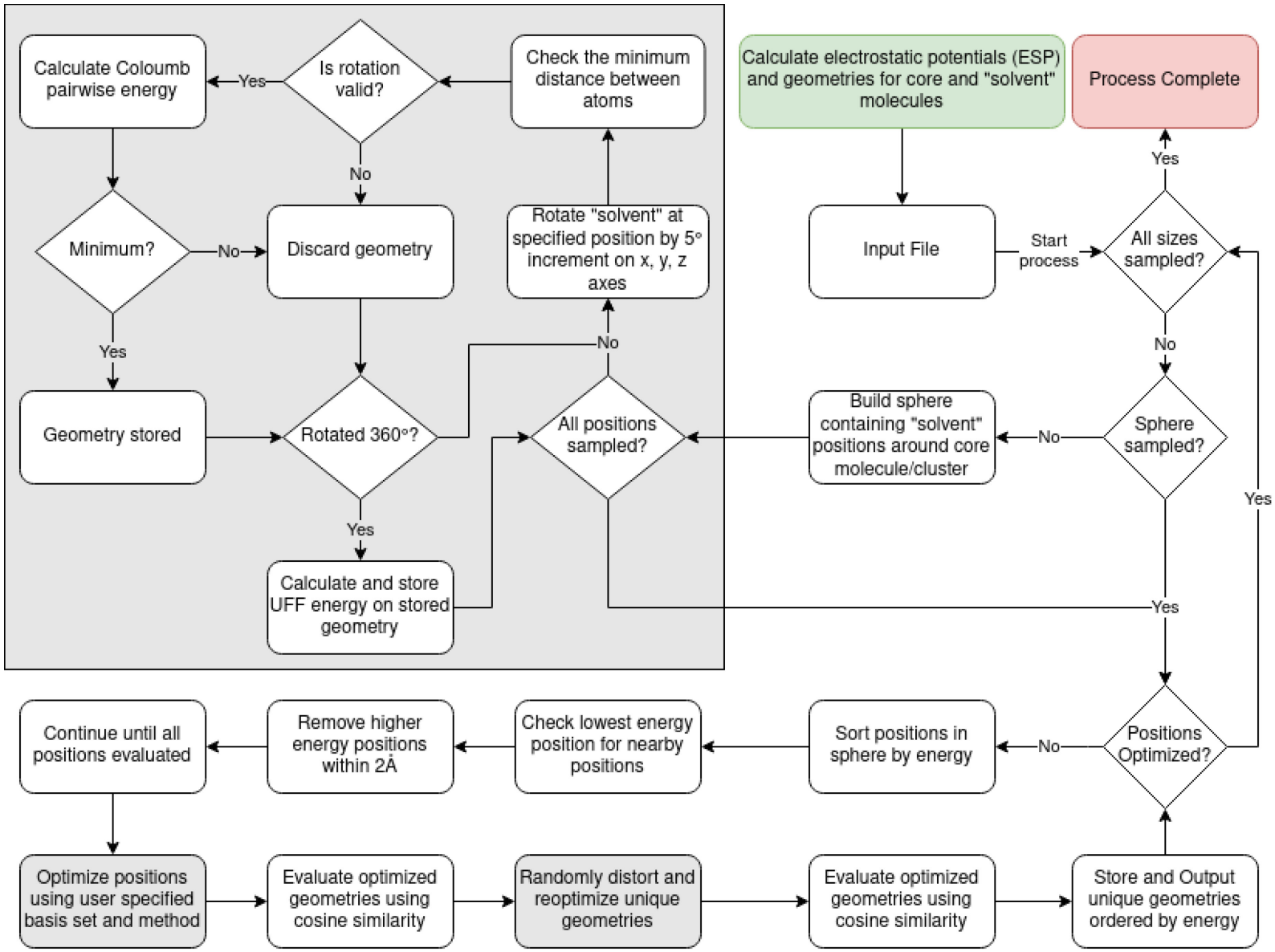

Figure S3-2. Workflow of the SSCS algorithm.

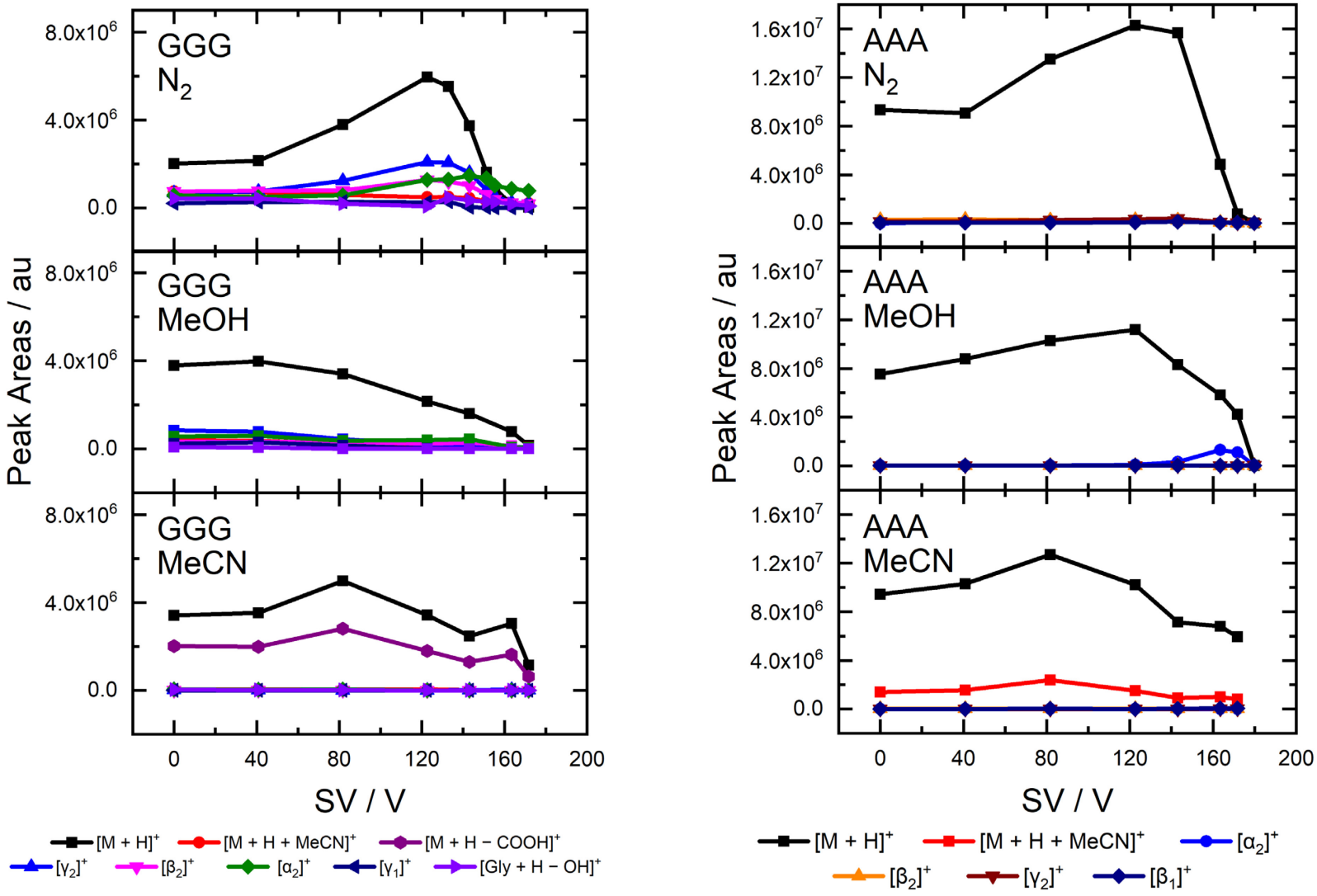

Figure S3-3. Peak areas of GGG (left) and AAA (right) and their corresponding fragments monitored as a function of SV (T_{bath} = 450 K).

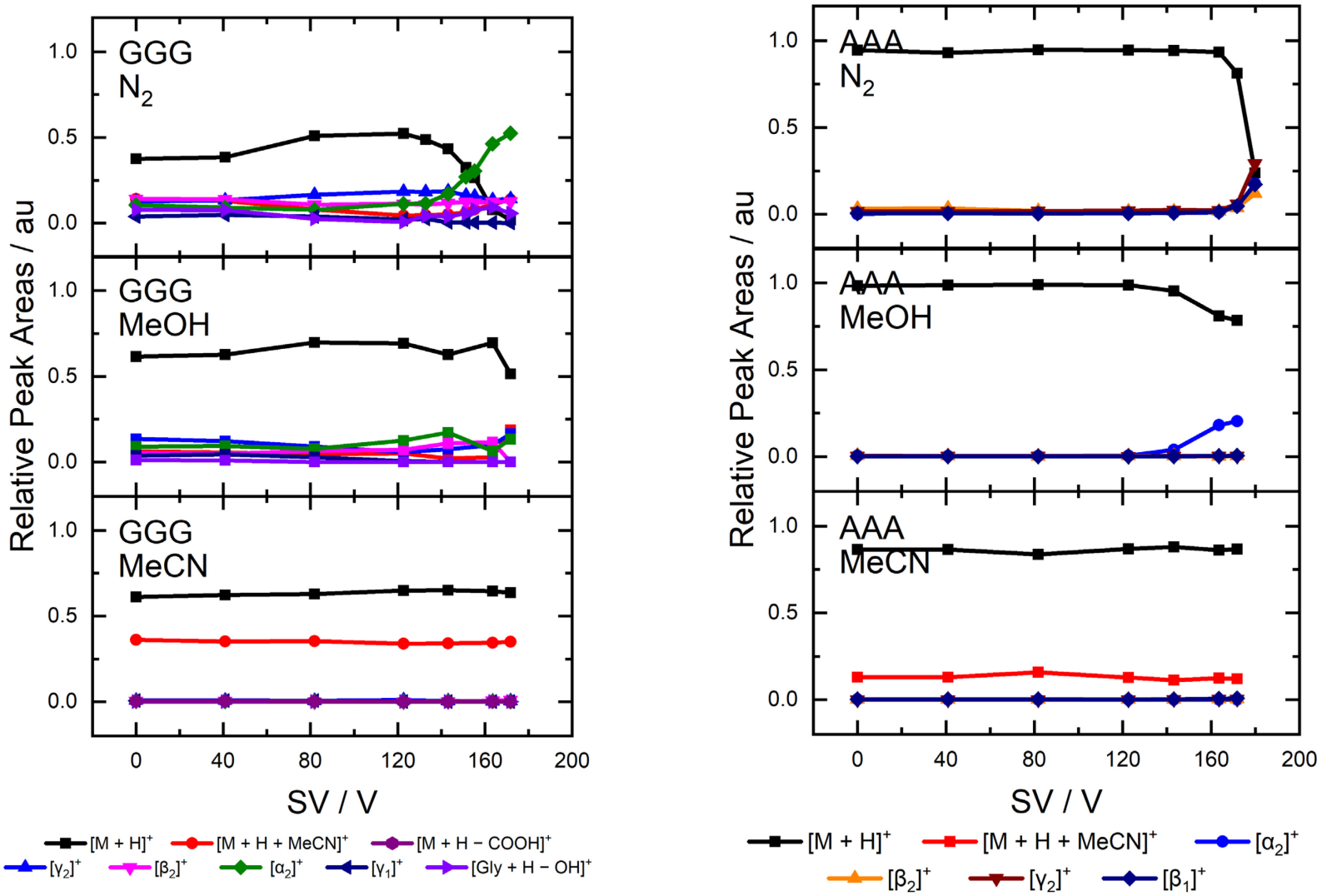

Figure S3-4. Peak areas of GGG (left) and AAA (right) and their corresponding fragments monitored as a function of SV (T_{bath} = 450 K) normalized to the total area of all ionograms peaks.

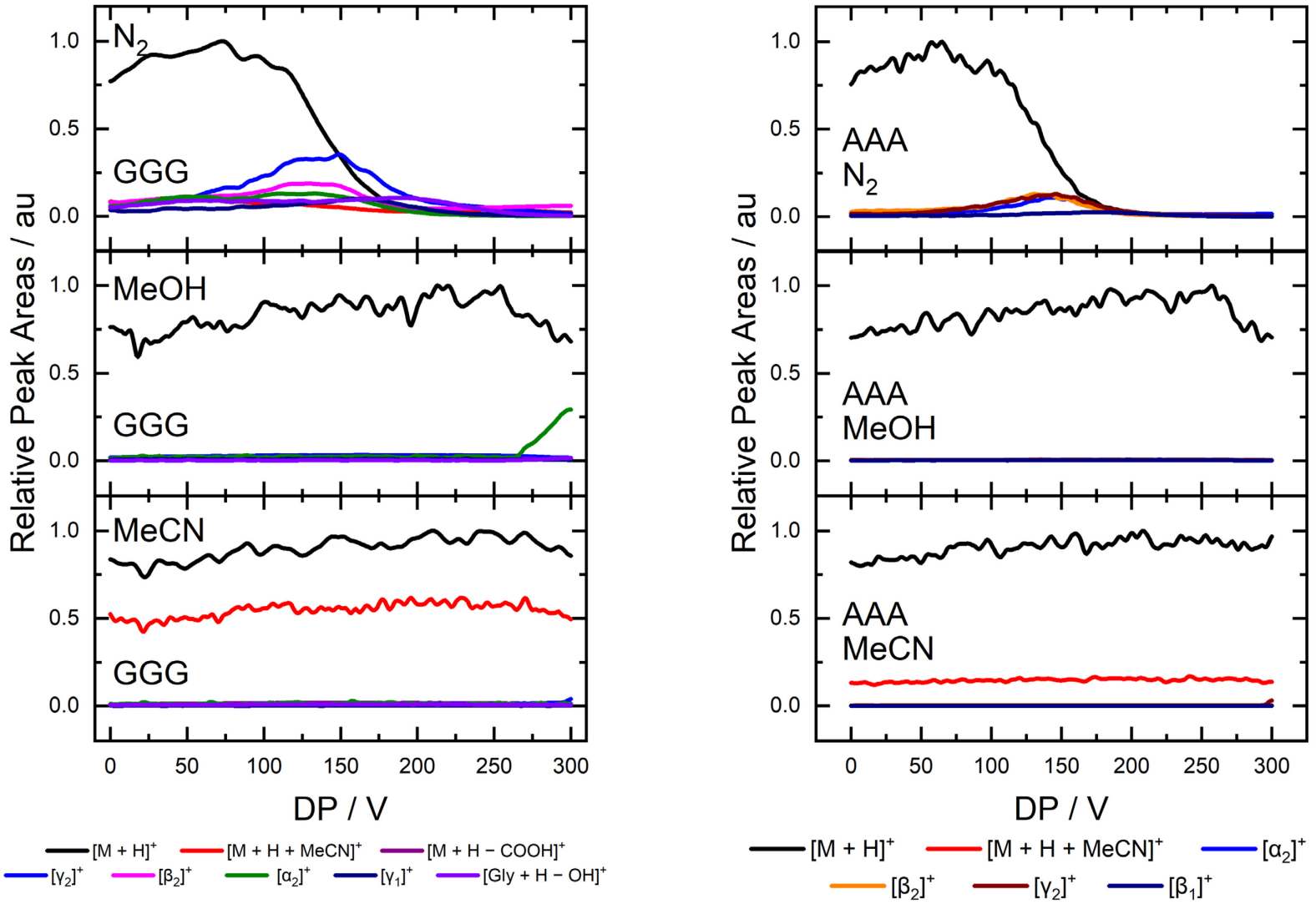

Figure S3-5. Stability of GGG (left) and AAA (right) towards up-front CID induced by application of a clustering potential In our N_2 (top panels), and N_2 seeded with 1.5 mol% of MeOH (middle panels) or MeCN (bottom panels).

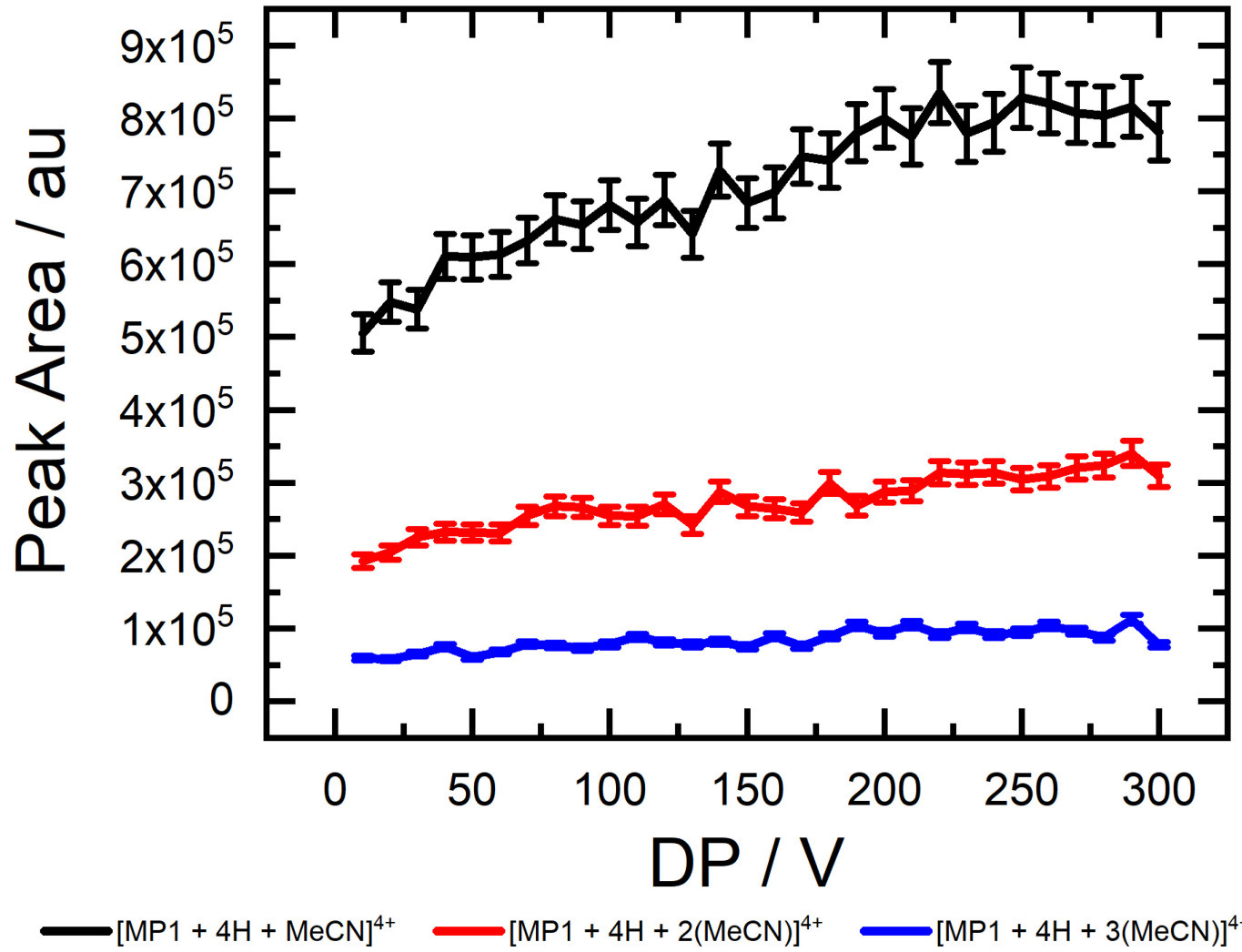

Figure S3-6. Stability of $[MP1 + 4H]^{4+}$ adducts with MeCN towards up-front CID induced by application of a declustering potential. Adducts are colour coded as follows: $[MP1 + 4H + MeCN]^{4+}$ (black); $[MP1 + 4H + 2(MeCN)]^{4+}$ (red); $[MP1 + 4H + 3(MeCN)]^{4+}$ (blue).

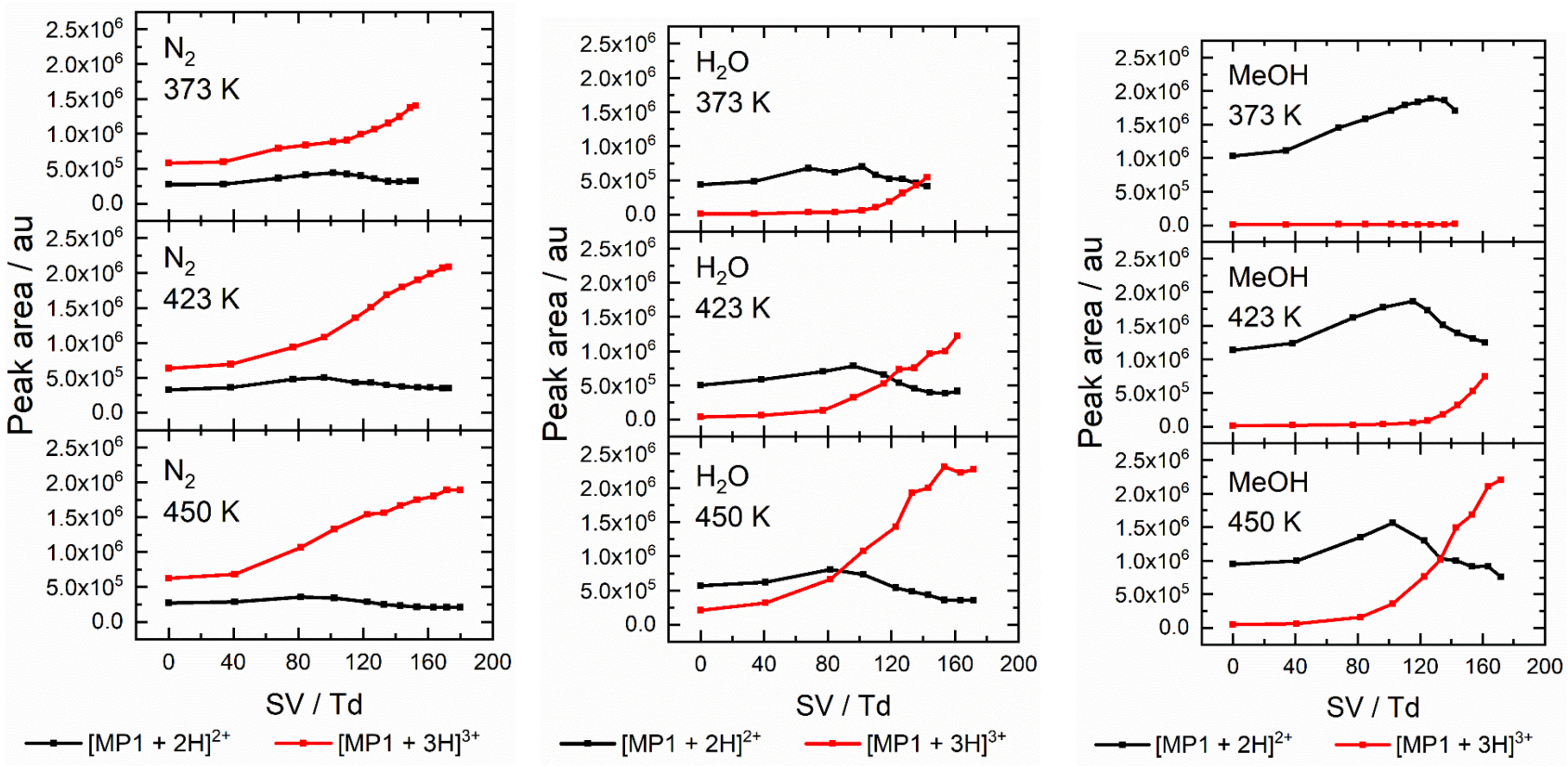

Figure S3-7a. Peak areas of $[MP1 + 2H]^+$ (black) and $[MP1 + 3H]^+$ (red) and their corresponding fragments monitored as a function of SV (T_{bath} = 450 K) normalized to the total area of all ionograms peaks.

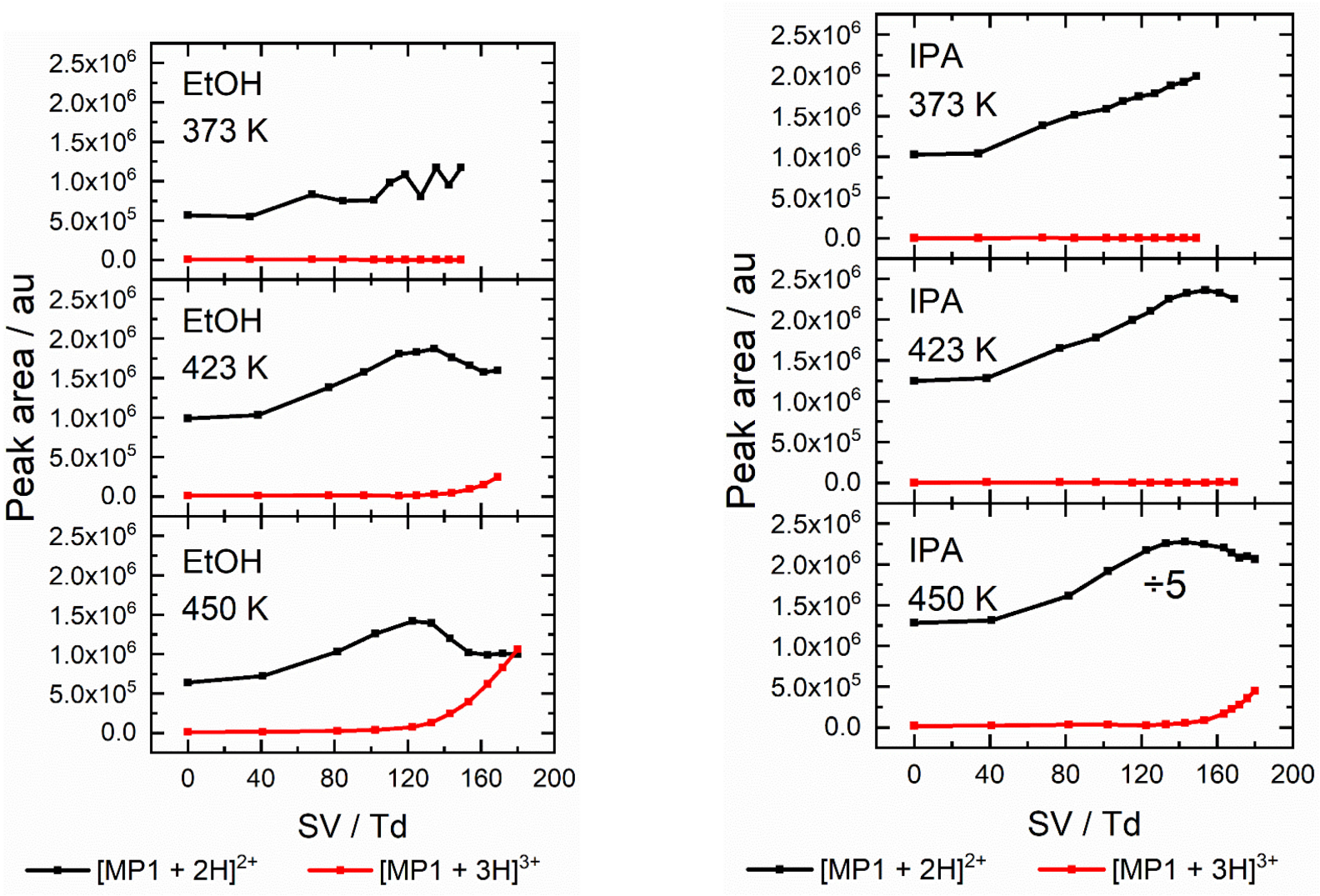

Figure S3-7b. Peak areas of $[MP1 + 2H]^+$ (black) and $[MP1 + 3H]^+$ (red) and their corresponding fragments monitored as a function of SV (T_{bath} = 450 K) normalized to the total area of all ionograms peaks.

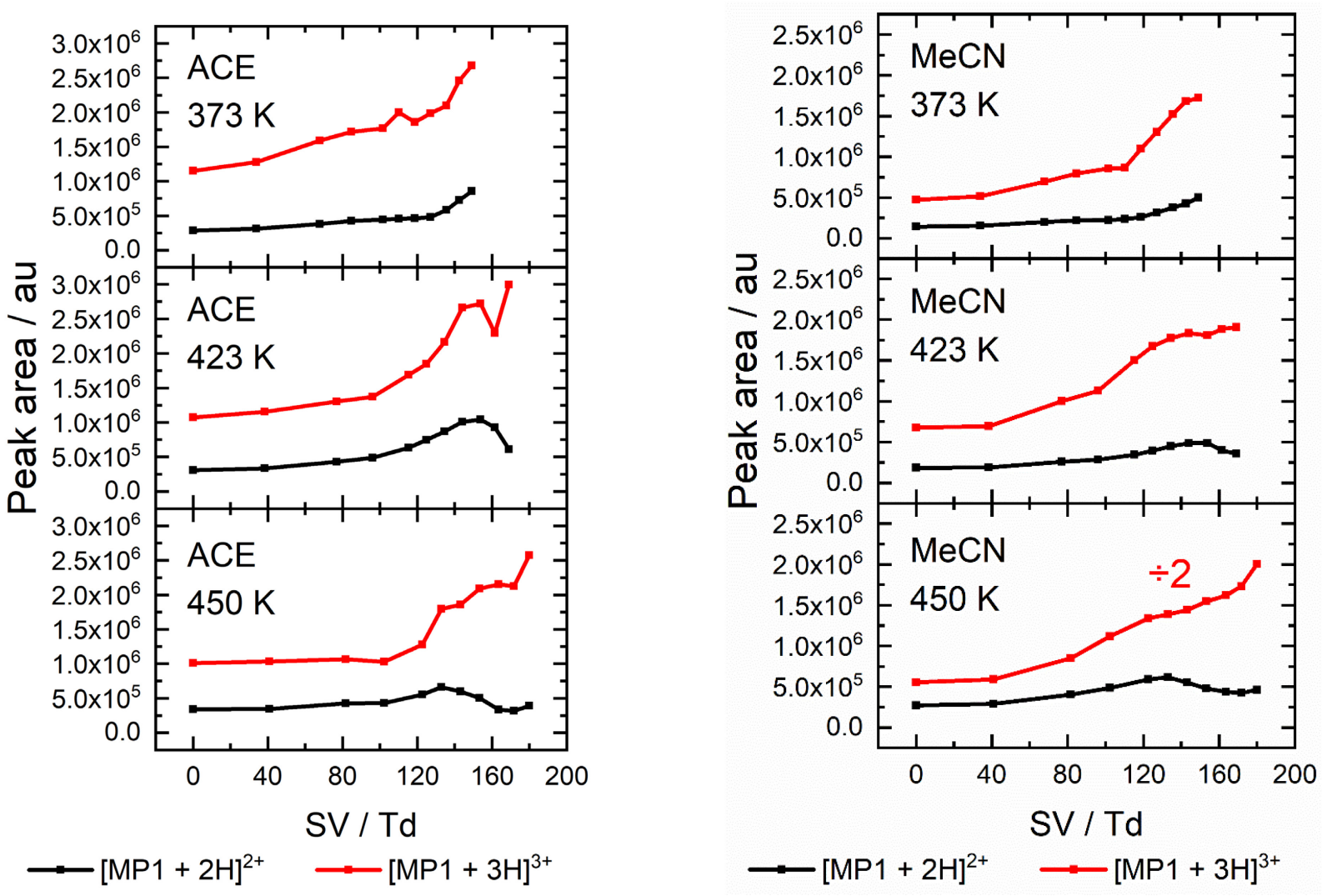

Figure S3-7c. Peak areas of $[MP1 + 2H]^+$ (black) and $[MP1 + 3H]^+$ (red) and their corresponding fragments monitored as a function of SV (T_{bath} = 450 K) normalized to the total area of all ionograms peaks.

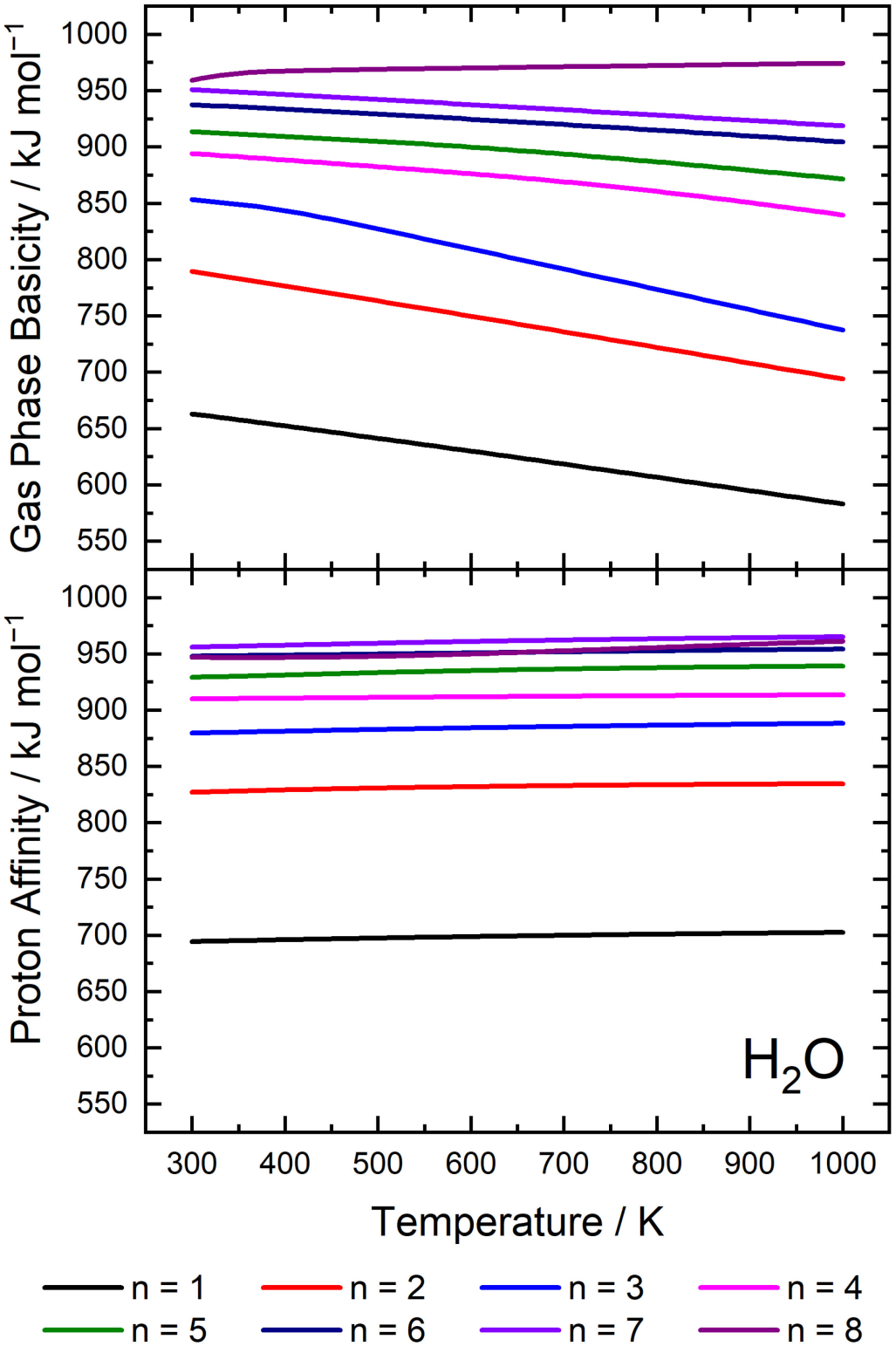

Figure S3-8. Gas-phase basicity and proton affinity for H_2O clusters of size *n*.

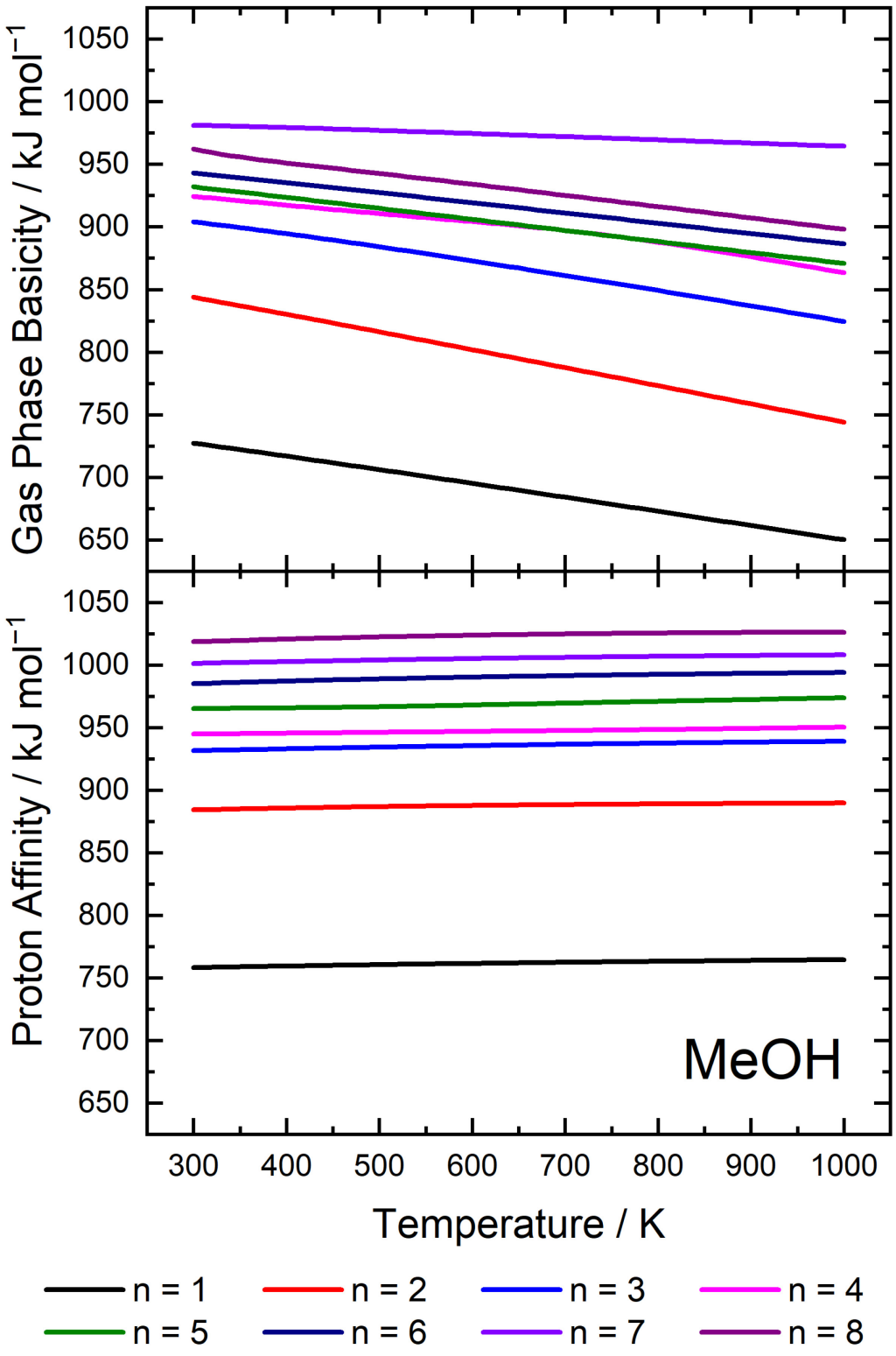

Figure S3-9. Gas-phase basicity and proton affinity for MeOH clusters of size *n*.

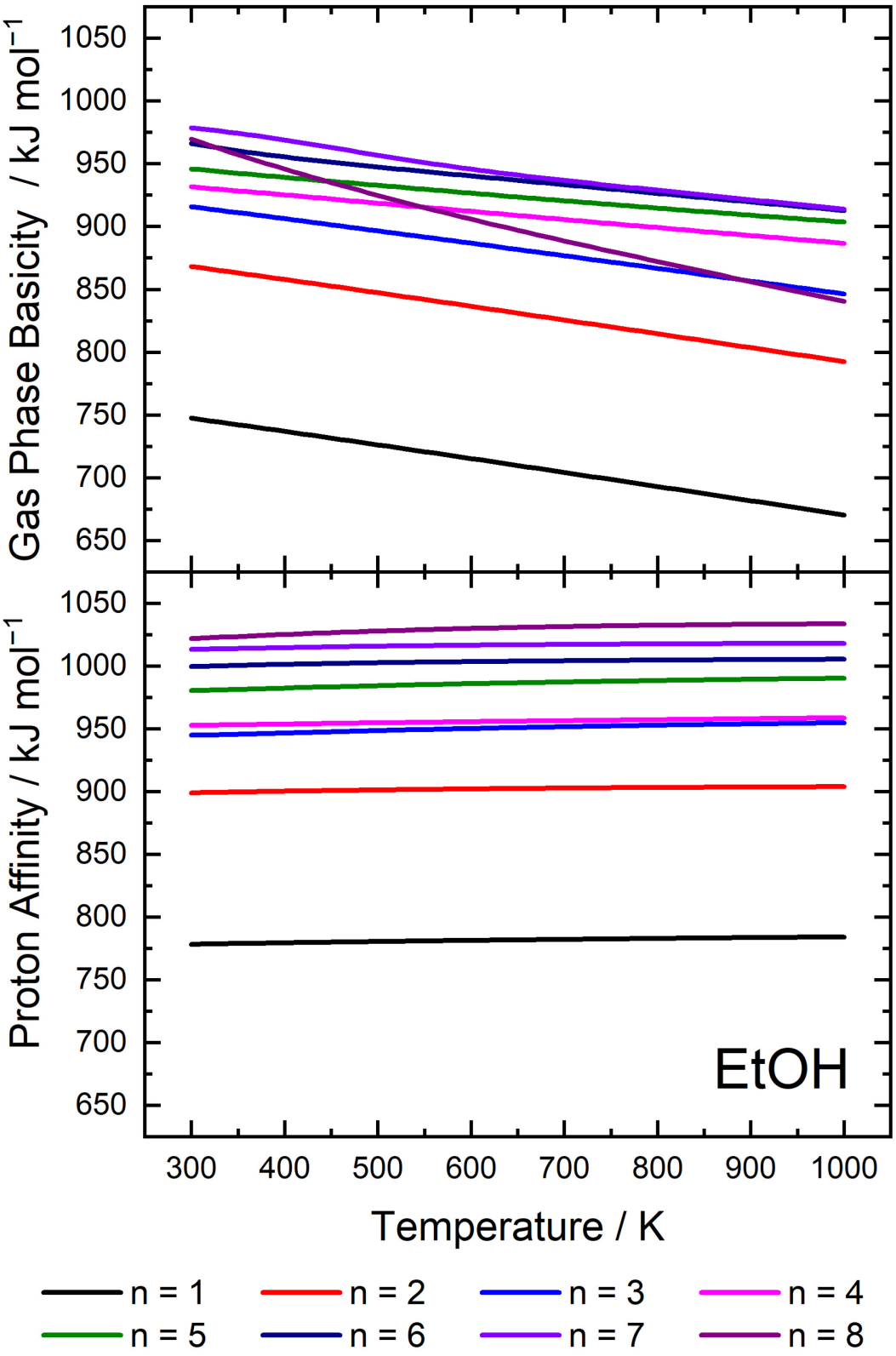

Figure S3-10. Gas-phase basicity and proton affinity for EtOH clusters of size *n*.

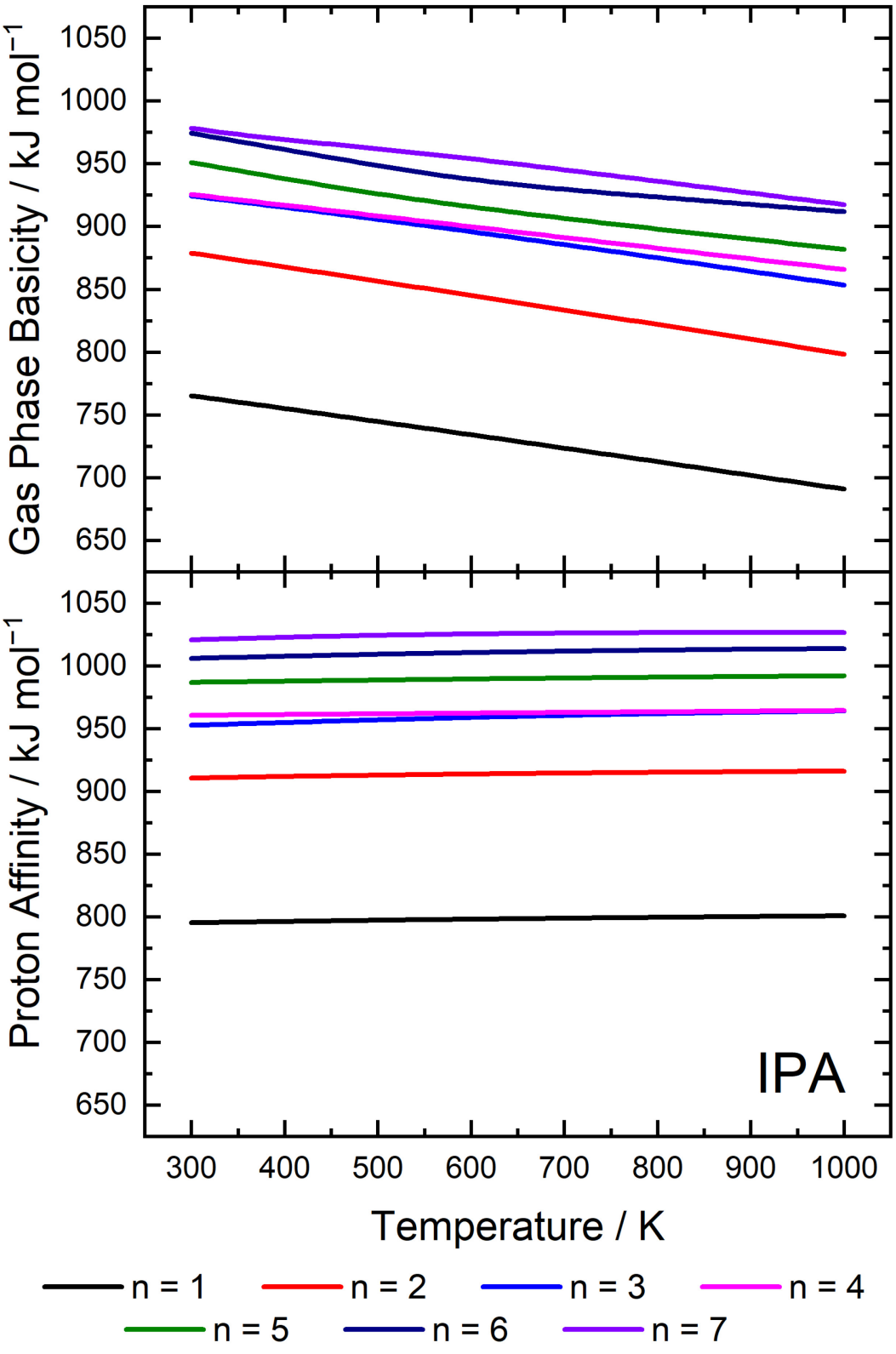

Figure S3-11. Gas-phase basicity and proton affinity for IPA clusters of size *n*.

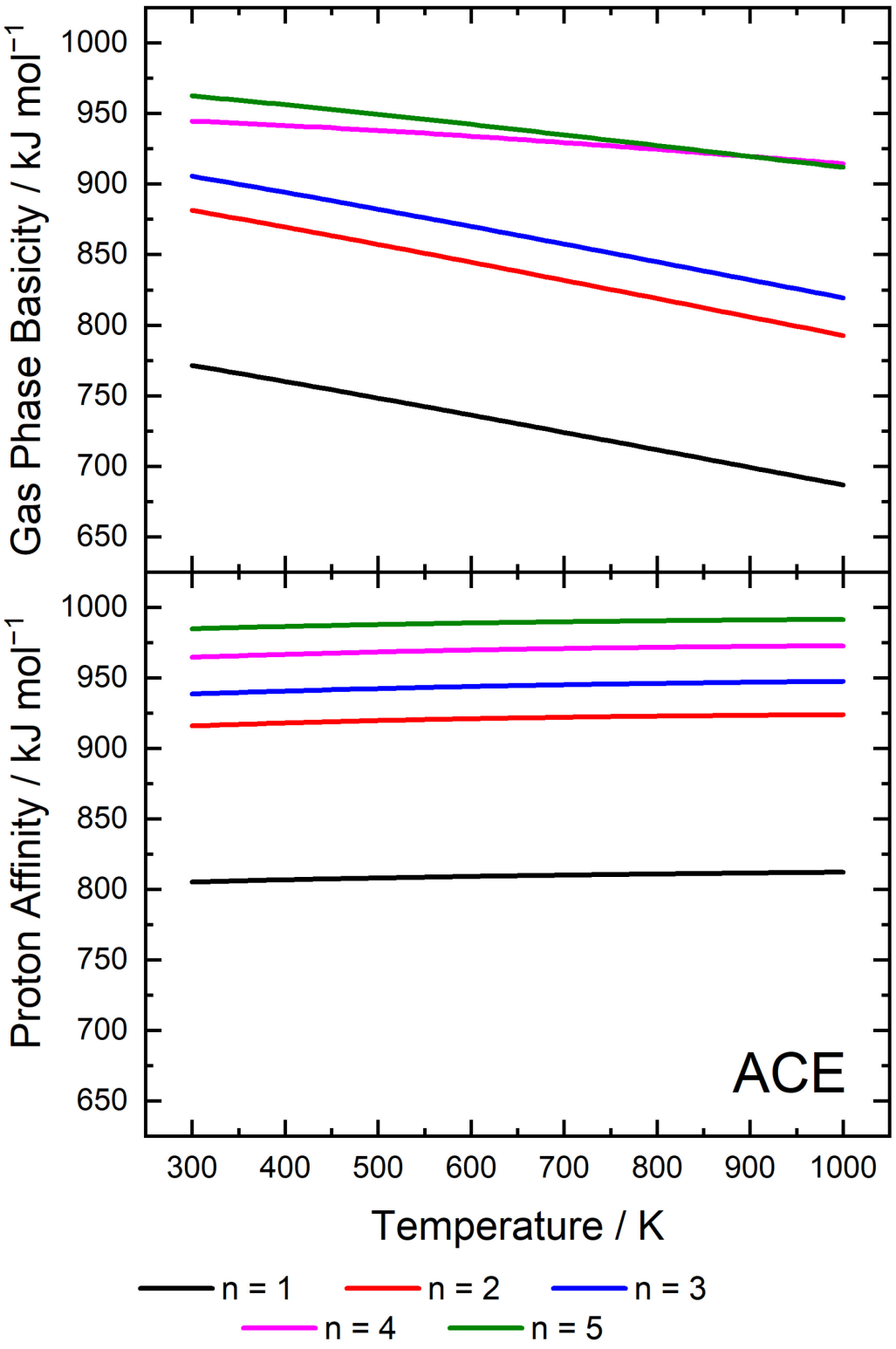

Figure S3-12. Gas-phase basicity and proton affinity for ACE clusters of size *n*.

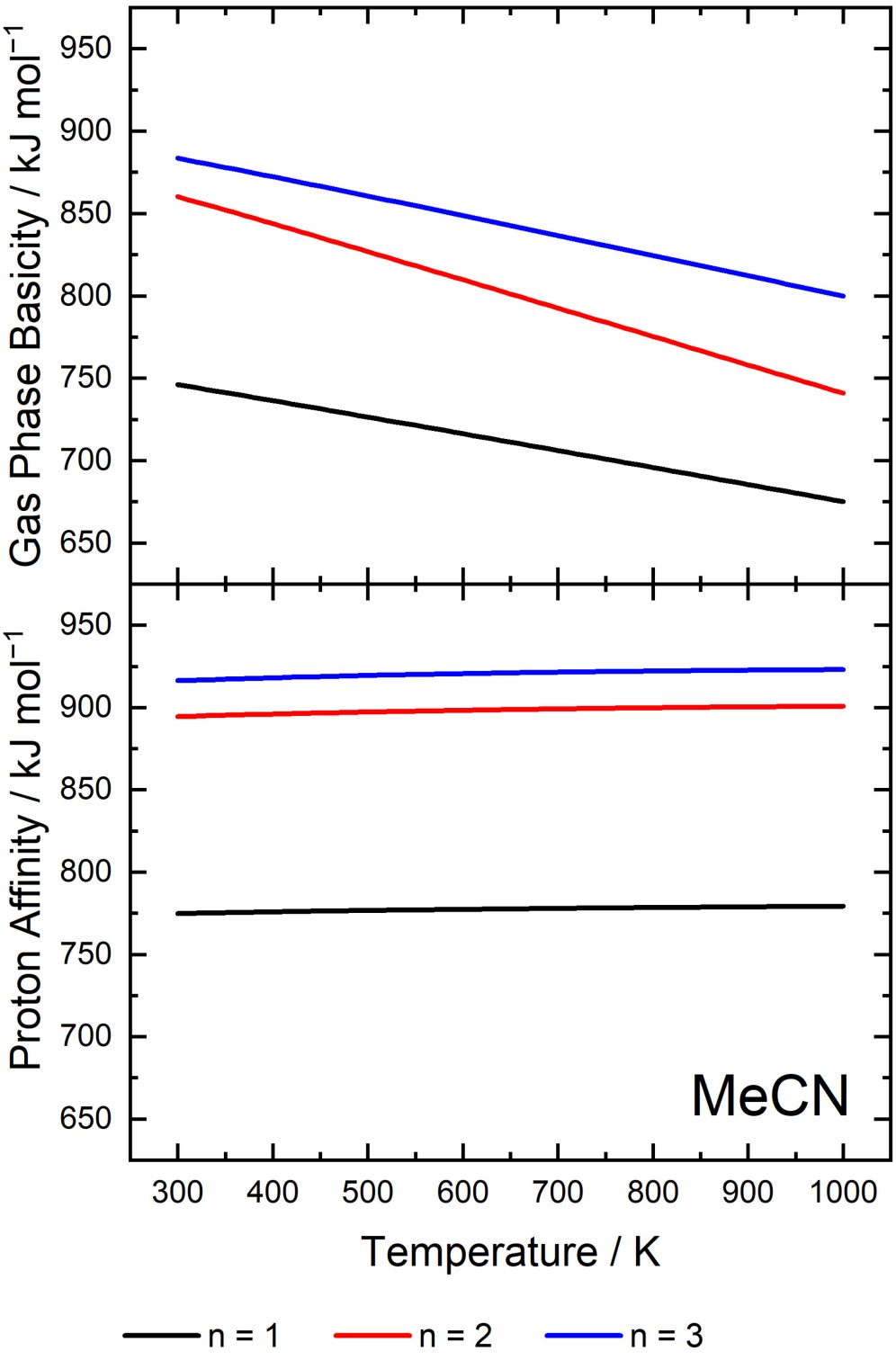

Figure S3-13. Gas-phase basicity and proton affinity for MeCN clusters of size *n*.

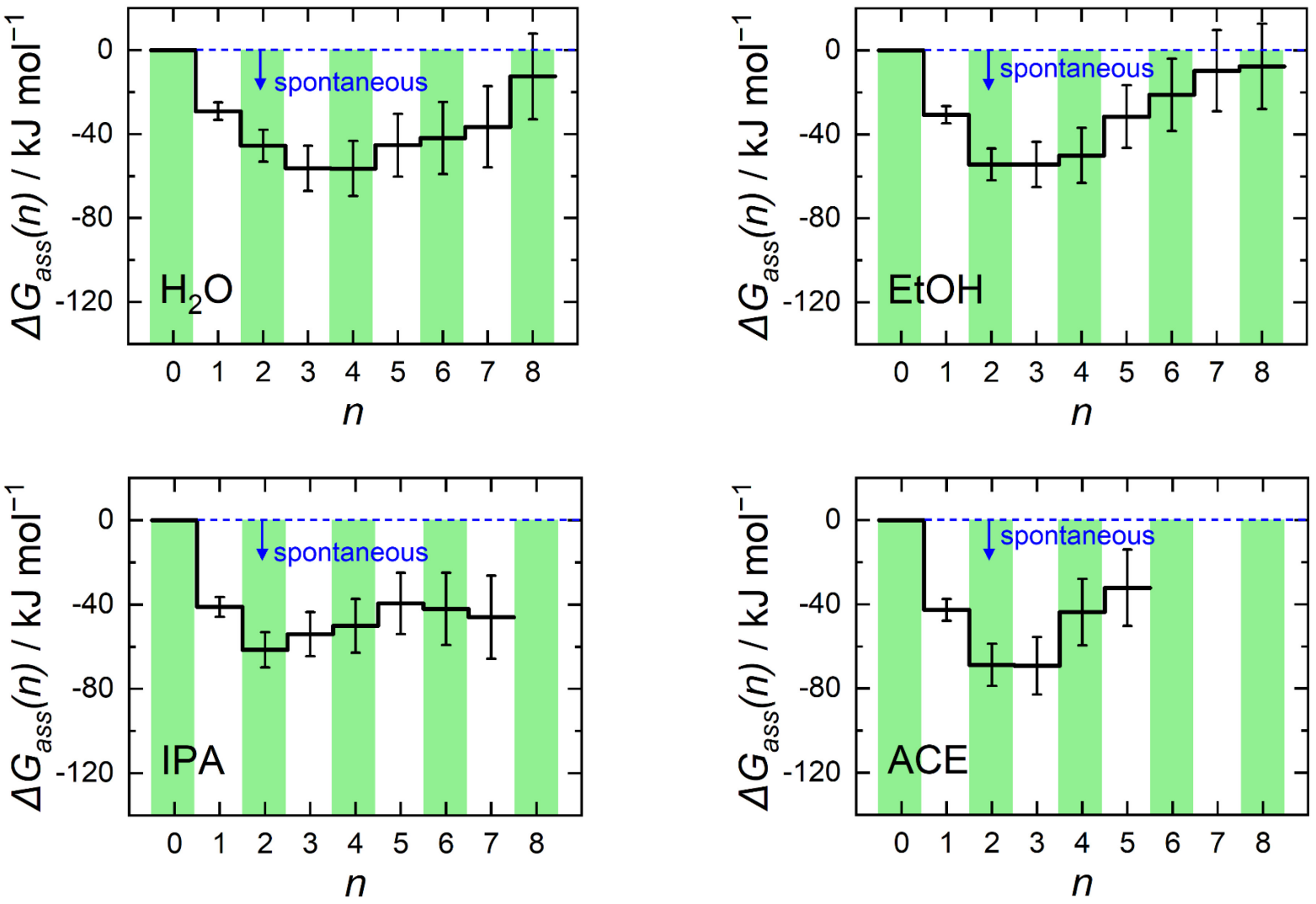

Figure S3-14. Gibbs energy of adduct formation (ΔG_{ass}) for each cluster size of H_2O, EtOH, IPA, and ACE ligated to $[PrNH_3]^+$. Values are calculated at 450 K and 1.00 atm. Error bars correspond to evaluation of ΔG_{ass} using scaling factors of 0.95 ± 0.05 for vibrational frequencies and propagation of 1.7 % RMSD in calculated Boltzmann weights.

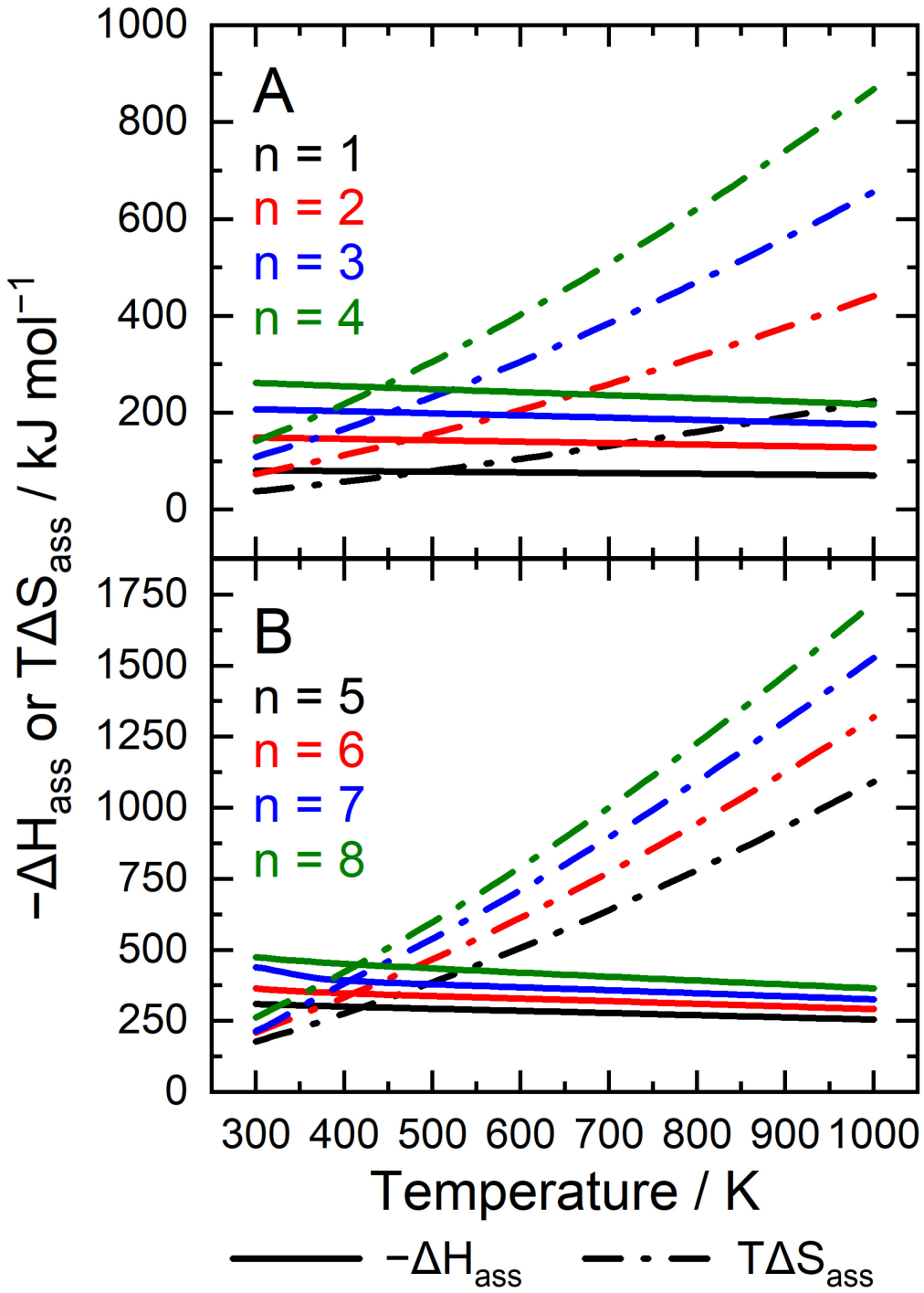

Figure S3-15. Negative enthalpic ($-\Delta H_{ass}$; solid line) and entropic ($T\Delta S_{ass}$; dashed line) contribution to the Gibbs energy of association for MeOH microsolvation of $[PrNH_3]^+$. Panel A depicts thermochemical quantities for cluster sizes of 1 (black), 2 (red), 3 (blue), and 4 (green); Panel B depicts thermochemical quantities for cluster sizes of 5 (black), 6 (red), 7 (blue), and 8 (green). Thermochemical quantities are determined using weighted enthalpies and entropies calculated from unscaled harmonic vibrational frequencies at a pressure of 1.00 atm

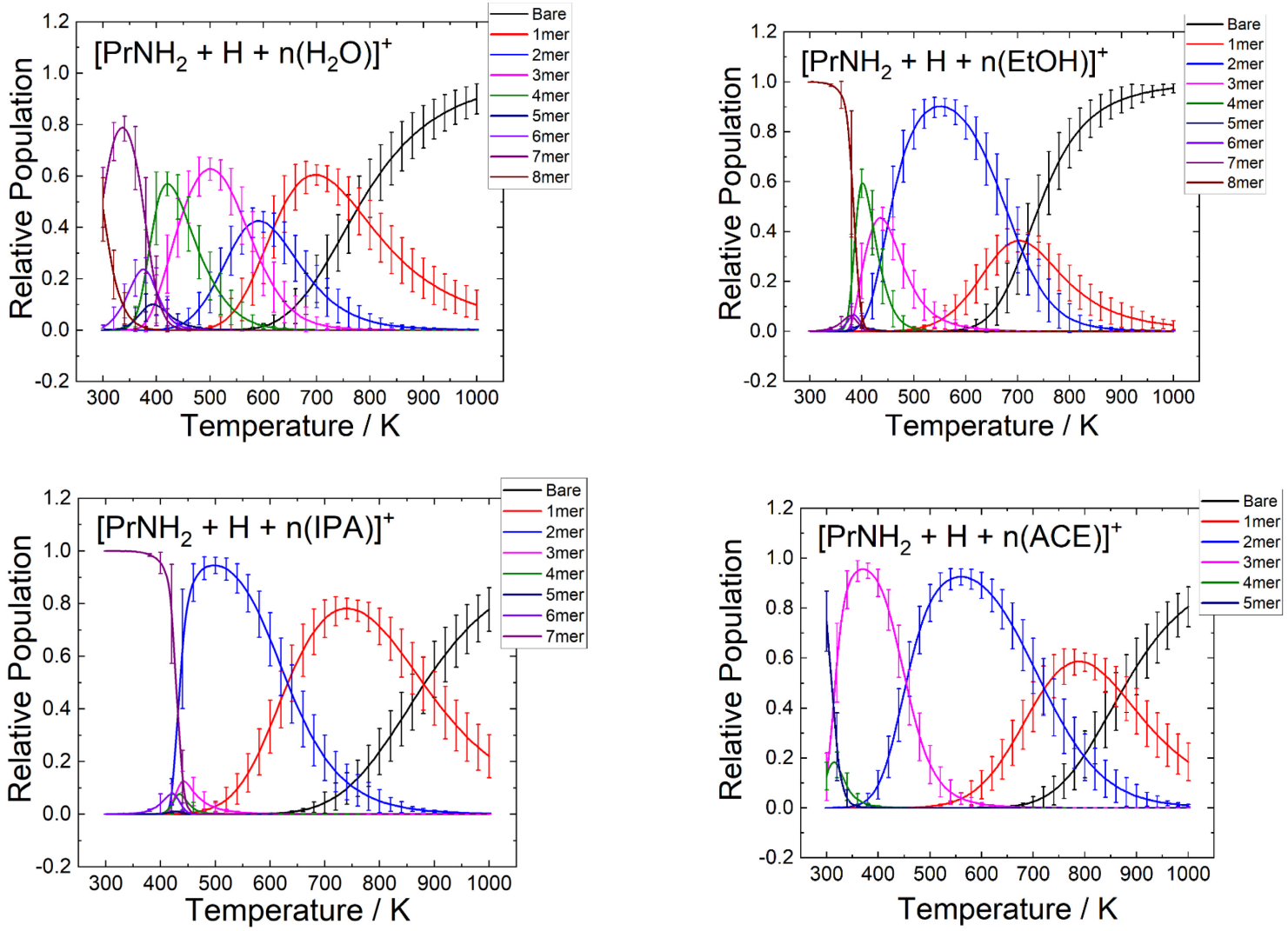

Figure S3-16. Relative populations (N_n) of microsolvated clusters of $[PrNH_3]^+$ with n H_2O, EtOH, IPA, or ACE molecules as a function of temperature (no solvent concentration included). Error bars correspond to evaluation of ΔG_{ass} using scaling factors of 0.95 ± 0.05 for vibrational frequencies and propagation of 1.7 % RMSD in calculated Boltzmann weights.

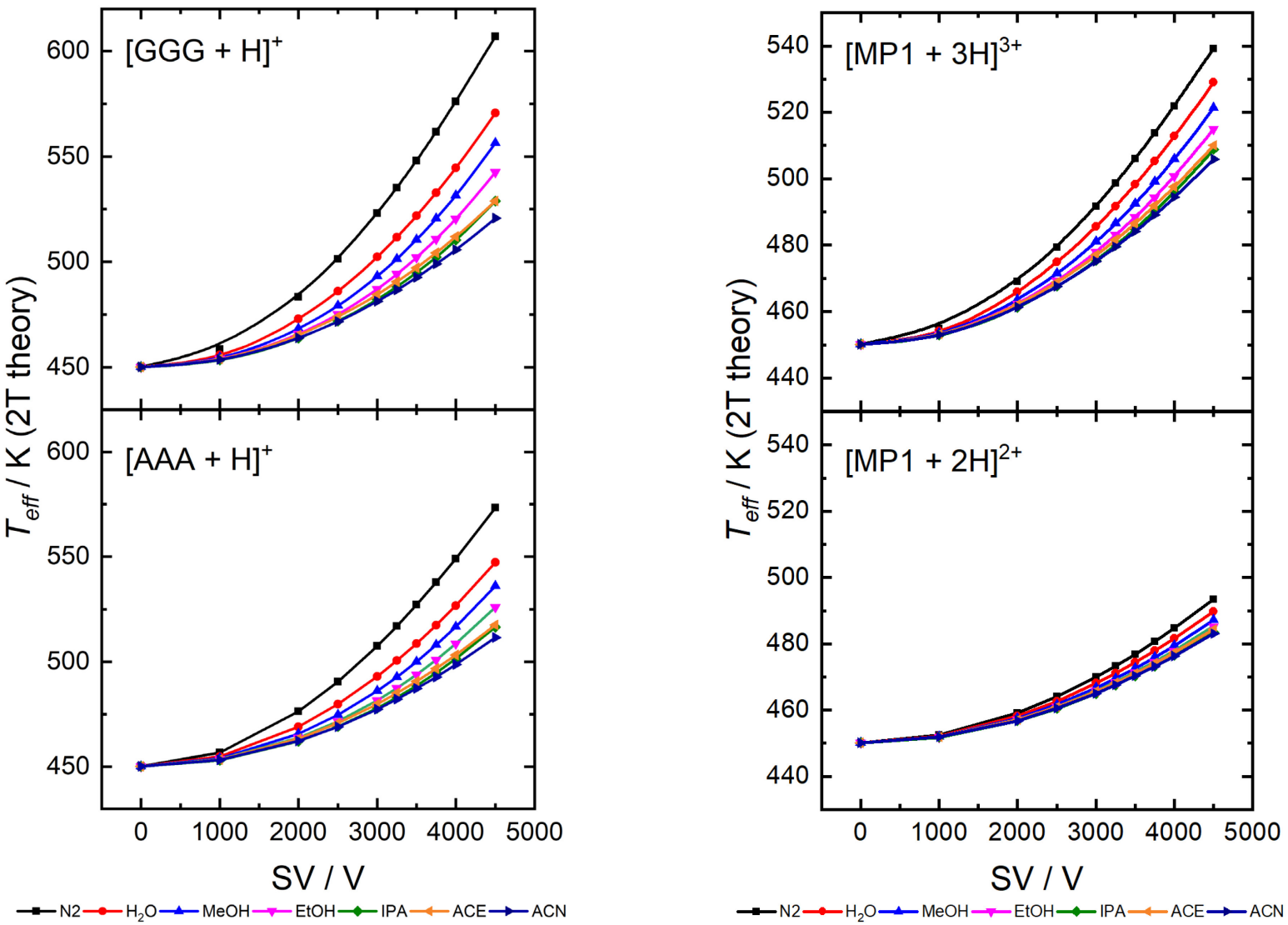

Figure S3-17. Evaluation of ion effective temperature (T_{eff}) at various separation field strengths using a modified self-consistent two-temperature theory approach to account for microsolvation (T_{bath} = 450 K).

Table S3-1. Comparison of the Proton Affinities (PAs) calculated at the MP2(full)/6-311++G(d,p)//ωB97X-D/6-311++G(d,p) level of theory to experiment.

PA	**MP2(full)/6-311++G(d,p)//ωB97X-D/6-311++G(d,p)**		**Experiment**[a]		**% dev**	
Size	**H_2O**	**MeOH**	**H_2O**	**MeOH**	**H_2O**	**MeOH**
1	694	758	699	761	-0.6	-0.4
2	827	884	816	883	1.4	0.2
3	880	932	862	937	2.0	-0.6
4	910	945	900	967	1.1	-2.2
5	929	965	904	979	2.8	-1.4
6	948	985	908	992	4.4	-0.7
7	956	1001		996		0.6
8	947	1019		1004		1.4
				RMSD:[b]		1.7

[a] PAs obtained from *Chem. Phys. Lett.* (1988), 144, 4, 317-323.

[b] Root mean square deviation

Supplementary sections for Chapter 3

Section S3-1: Microsolvated geometries of $[PrNH_3]^+$ with MeOH and MeCN

Microsolvated structures of $[PrNH_3]^+$ were calculated for H_2O, MeOH, EtOH, and IPA. Figure S3-18 shows the global minimum structures (with respect to Gibbs corrected energies) for $[PrNH_2 + H + n(MeOH)]^+$ ($n = 1 - 8$) clusters as a representative sample for protic solvents. For all microsolvated clusters containing protic species, solvent aggregates adopt hydrogen-bonding networks centered around the charge site. Up to $n = 3$, MeOH molecules coordinate to each free H-bond donor of the $[NH_3]^+$ moiety. As n increases, closed hydrogen bonding networks become increasingly favourable.

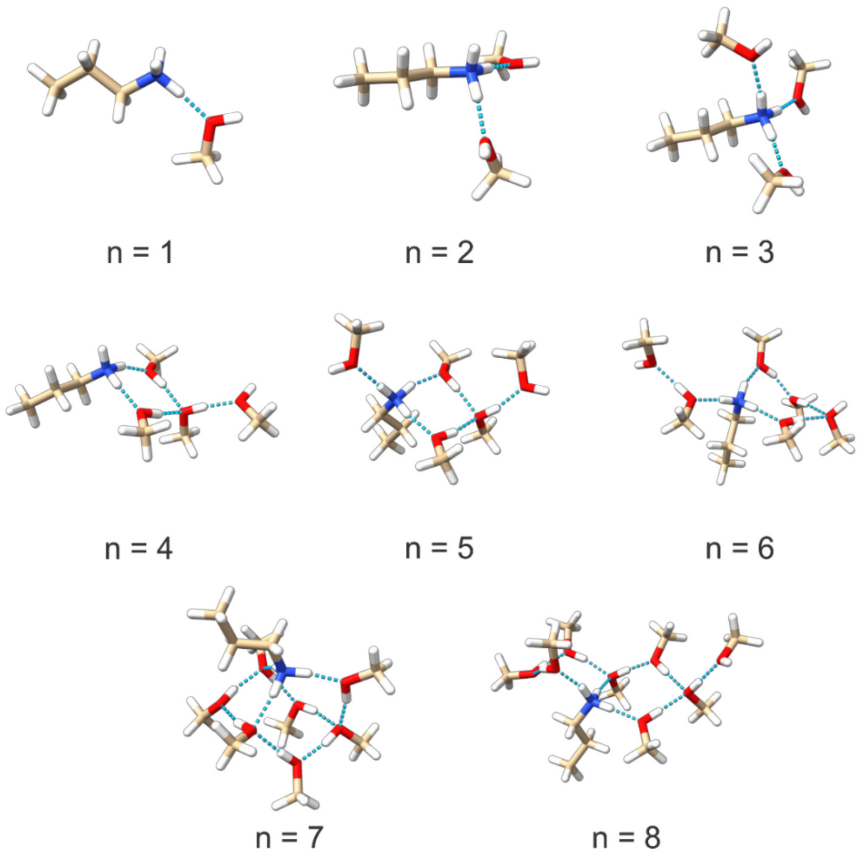

Figure S3-18. Global minimum structures of $[PrNH_3 \cdot \cdot \cdot (MeOH)_n]^+$ (n = 1 – 8) based on standard Gibbs corrected energies calculated at the MP2(full)/6-311++G(d,p)//ωB97X-D/6-311++G(d,p) level of theory.

The extensive hydrogen-bonding that occurs in protic solvent clusters containing $[PrNH_3]^+$ has important bearings on the fate of the ion swarm within the DMS cell. Mechanisms for proton transfer are often rationalized using a Grotthuss-like process,[1] where the proton migration occurs through the hydrogen bonding network. Depending on the location of the proton, fragmentation of the solvent cluster from the microsolvated aggregate can result in charge stripping. However, the distribution of cluster sizes and the nature of the proton transfer reaction will determine whether charge depletion or charge retention occurs. Ion temperature is crucial in determining which pathway will be followed, as the size of solvent clusters that accrete onto charged analyte is largely governed by entropic effects.

The nature of the microsolvated cluster must also be taken into consideration. Consider the global minimum structures of $[PrNH_3]^+$ microsolvated with MeCN shown in Figure S3-19. With only a single H-bond acceptor available on the solvent ligand, MeCN can only interact with the charge site directly through coordination of one of the three available protons on $[PrNH_3]^+$. For cluster sizes larger than $n = 3$, coordination of subsequent MeCN moieties occurs either in the vicinity of the protonated amine or through interaction with another MeCN molecules.

The lack of hydrogen bond donors in aprotic modifiers has a significant impact on whether charge retention or proton abstraction will occur. For example, since MeCN clusters cannot form extended hydrogen bond networks, proton transfer must occur to a single MeCN molecule. Despite the increased GPB of solvent clusters compared to the bare molecule,[2–5] aprotic modifiers clustered at the charge site must undergo extensive geometrical rearrangements to transfer a proton from the $[PrNH_3]^+$ core to the solvent cluster. This rearrangement was shown to be associated with high activation barriers by Haack and coworkers.[6] Thus, aprotic modifiers promote charge retention due to their high affinity to the charge site and hindered proton transfer, which has important connotations toward stabilizing multiply charged ions. To garner insight into the microsolvation process, the populations of ion-solvent clusters and the propensity of the analyte towards microsolvation were examined.

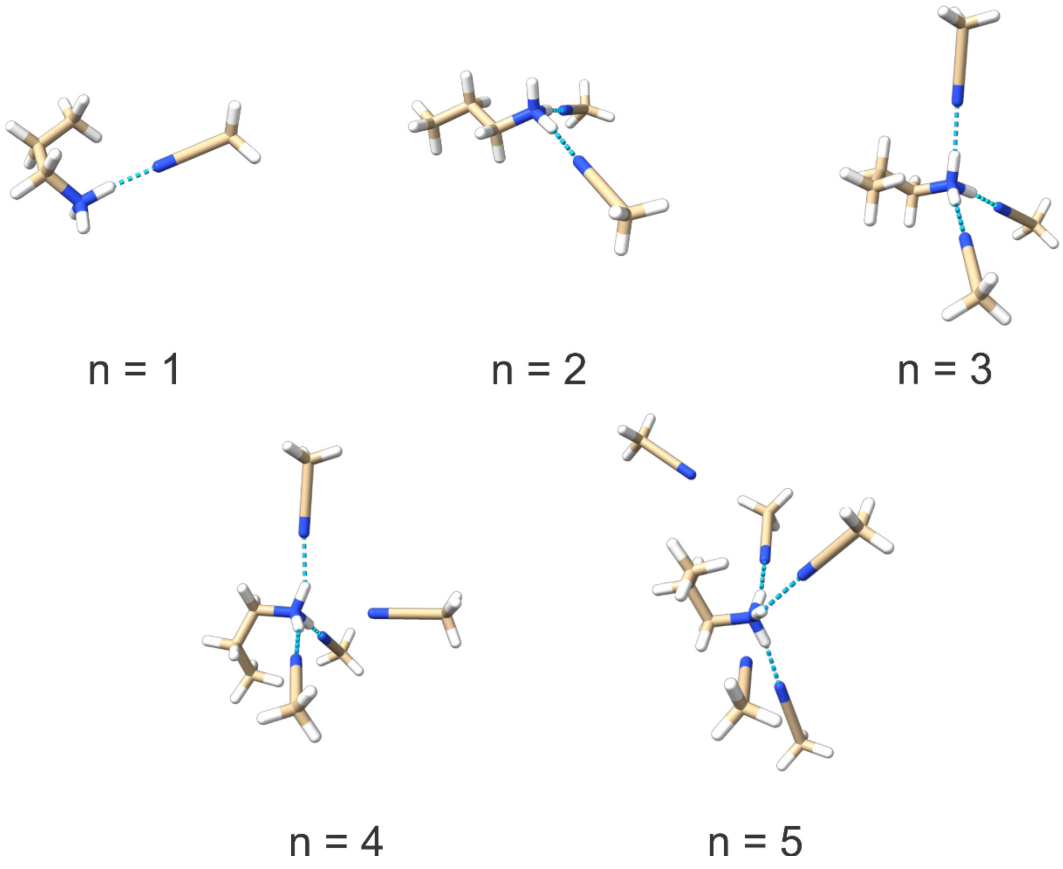

Figure S3-19. Global minimum structures of $[PrNH_3 \cdot \cdot \cdot (MeCN)_n]^+$ (n = 1 – 5) based on Gibbs corrected energies at the MP2(full)/6-311++G(d,p)//ωB97X-D/6-311++G(d,p) level of theory.

Section S3-2: Modifications to ion-solvent cluster population to account for solvent concentration

A modification based on formalisms present in literature can be applied to yield equation S1,[7,8] where *[M]* is the solvent concentration, N is the particle density, and n_n is the number of solvent ligands coordinated to the analyte.

$$N_n(T) = \frac{\left(\frac{[M]}{N}\right)^{n_n} \exp\left(-\frac{\Delta G_{rel\_ass,n}(T)}{RT}\right)}{\sum_n \left(\frac{[M]}{N}\right)^{n_n} \exp\left(-\frac{\Delta G_{rel\_ass,n}(T)}{RT}\right)} \qquad \textit{Eq S1}$$

Microsolvated cluster populations determined using equation S1 (1.5 mol% concentration of solvent modifier) are shown in Figure S3-20. Populations of $[PrNH_2 + H + n(Solv)]^+$ are found to have a maximum cluster size of $n = 4$ under 'soft' DMS conditions (T_{bath} = 373 K, SV < 50 Td). Microsolvated populations predicted by equation 8 at any modest separation field strength or elevated bath gas temperatures (*e.g.,* 450 K) yields cluster sizes of $n = 2$, which is inconsistent with observations in this study. This inconsistency arises due to the detection of the $[MP1 + 3H]^{3+}$ in a DMS environment seeded with MeOH (Figure 3 in main text), which occurs at T_{bath} = 450 K and SV > 75 Td ($2.0 \cdot 10^6$ V · m^{-1}). This corresponds to an effective ion temperature of *ca.* 460 K (*vide infra*). A mechanistic appraisal of the solvent-mediated proton abstraction of $[MeNH_3]^+$ was conducted by members of the Benter group,[6,9] which suggested that at least three MeOH molecules are required to remove a proton. Population analysis using equation S1 indicates that each amine is solvated by one and two methanol molecules at 460 K. Since charge stripping is not possible with microsolvated clusters of $n \leq 2$, the ion population should predominantly be composed of the $[MP1 + 3H]^{3+}$ protomer. However, only 10 % of the ion population measured experimentally consists of $[MP1 + 3H]^{3+}$ at T_{bath} = 450 K and SV = 75 Td. This suggests that microsolvated cluster populations are underestimated by equation S1.

This is further evident when modelling differential ion mobility in solvent modified carrier gases (*cf.* Figure 7a in ref. 7). Dispersion plots of Me_4N^+ in 1.5 mol% of MeOH approach experimental observations as the concentration of solvent modifier is increased. The systematic underestimation of microsolvated cluster size is likely caused by the accuracy of the model chemistry employed and, in particular, by the calculating thermochemical quantities using harmonic vibrational frequencies. Spectroscopic investigations show that vibrational frequencies derived from harmonic models do not accurately capture vibrations in systems dominated by hydrogen bonding.[10–12] This becomes increasingly problematic with increasing size of the microsolvated cluster. As a result, ΔG_{ass} will underestimate the populations of larger cluster sizes.

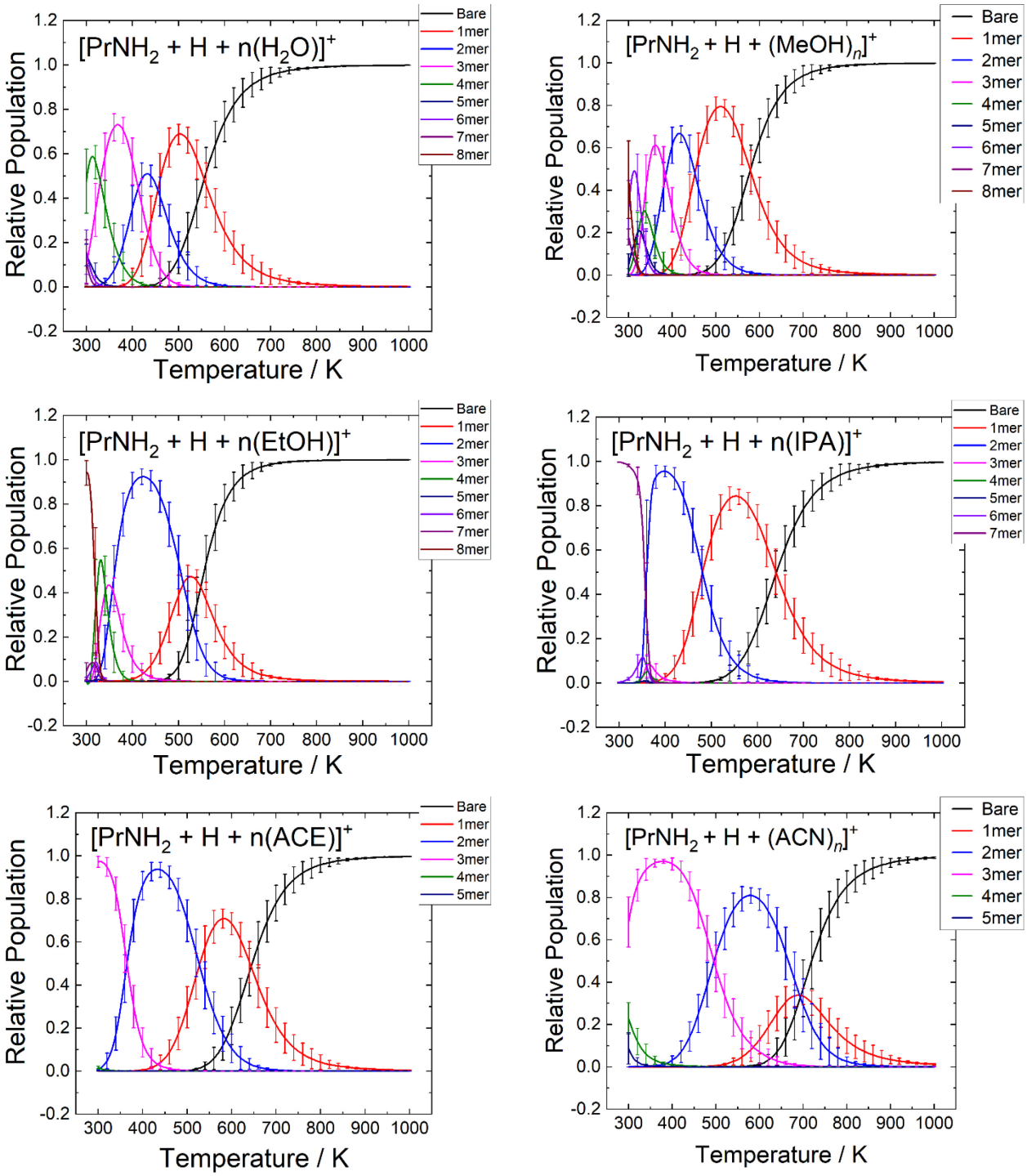

Figure S20. Relative populations (N_n) of microsolvated clusters of $[PrNH_3]^+$ with n H_2O, EtOH, IPA, or ACE molecules as a function of temperature with a 1.5 mol% concentration of solvent modifier. Error bars correspond to evaluation of ΔG_{ass} using scaling factors of 0.95 ± 0.05 for vibrational frequencies and propagation of 1.7 % RMSD in calculated Boltzmann weights.

With anharmonic calculations being prohibitively expensive, subsequent discussions of ion-solvent cluster populations and stabilizing effects are derived from equation 7 in the main text, which does not have a dependence on solvent concentration. The errors associated with these populations should, to some degree, cancel the underestimation of solvent cluster population and inadequate treatment of vibrational frequencies with a harmonic model.

Section S3-3: Modifications to two-temperature theory accounting for microsolvation

Modifications to the Mason-Schamp relation (equation S2) to mimic the mobility shifts incurred due to solvent accretion are shown below,

$$K = \frac{\sqrt{18\pi}}{16}\sqrt{\frac{1}{m_{ion}(T)}+\frac{1}{m_{gas}}}\left(\frac{ze}{\sqrt{k_b T}}\right)\left(\frac{1}{\Omega(\mathrm{T})}\right)\left(\frac{1}{N}\right) \qquad \textit{Eq S2}$$

where $m_{ion}(T)$ is the mass of the microsolvated cluster at temperature T, m_{gas} is the molecular mass of the buffer gas, z is the charge, e is the elementary charge, k_b is the Boltzmann constant, N is the number density of the gas, $\Omega(T)$ is the CCS at temperature T, and K is the ion mobility. Modifications include functional fits to describe the temperature dependence of the microsolvated cluster's mass and CCS. To model the increase in the microsolvated cluster's mass, the mass increase ($m_{inc}(T)$) is generated as a function of temperature (equation S3), which is governed by the relative population of $[PrNH_3]^+$ with n solvent ligands at temperature T (N_n, equation 5 in the main text) and the mass of the free solvent modifier (m_{solv}). The mass increase is added to the mass of the bare analyte (m_{ion}) and weighted by the sum of the solvent accessible surface area (SASA) of the i^{th} amino containing residue, which is represented as the average SASA determined over the course of a 200 ns NVT molecular dynamics (MD) simulation at 500 K (equation S4). MD simulations are performed for

$[GGG + H]^+$, $[AAA + H]^+$, $[MP1 + 2H]^{2+}$ (6 prototropic isomers), and $[MP1 + 3H]^{3+}$ (4 prototropic isomers). The SASA of the amino-containing moiety is compared to the SASA of free $[PrNH_3]^+$ ($SASA_{free}$), which is determined from an identical MD simulation protocol; full details of the MD work can be found in the dedicated section within the supplementary information (Table S7).

$$m_{inc}(T) = \sum_n \big(N_n(T)\big)\big((n)(m_{solv})\big) \qquad \textit{Eq S3}$$

$$m_{ion}(T) = m_{ion} + \big(m_{inc}(T)\big) \sum_i \left(\frac{SASA_i}{SASA_{free}}\right) \qquad \textit{Eq S4}$$

In a similar manner, the increase in CCS can be modelled using the relative populations of the microsolvated clusters. Ion mobility was evaluated using temperature-dependant CCS calculations in N_2 ($\Omega(T)$) performed in MobCal-MPI.[13] The CCS of the bare analyte was determined by taking the lowest energy structure from each MD run of the respective peptide and performing a geometry optimization at the B3LYP/6-31G(d) level of theory. DFT calculations included the GD3 empirical dispersion correction.[14] Normal mode analyses were conducted to verify that each isomer corresponded to a minimum on the PES. Atomic partial charges were generated according to the Merz-Singh-Kollman (MK) partition scheme,[15,16] and constrained to reproduce the dipole moment of the peptide.

Calculated ion CCSs at a specific temperature ($\Omega(T)$) were modified according to the size of the microsolvated clusters using equations S5 and S6. The increase in CCS ($\Omega_{inc}(T)$) is determined from the difference in CCSs of the $[PrNH_3 \cdot \cdot \cdot (Solv)_n]^+$ clusters ($\Omega_{PrNH3 \cdot (Solv)n}(T)$) and the bare $[PrNH_3]^+$ cation ($\Omega_{PrNH3}(T)$), weighted by the population of the cluster size n (N_n). As before, ($\Omega_{inc}(T)$) is weighted by the sum SASA of the i^{th} amino containing residue and added to the CCS of the bare analyte ($\Omega_{ion}(T)$) to give $\Omega(T)$. $\Omega(T)$s were fit to a function of the form $a + b(T_{eff})^c$, which is based on the proportionality of CCS to $T^{-1/2}$ in the low-field limit. Functional fits of both mass and CCS increase are provided in the dedicated section within the supplementary information.

$$\Omega_{inc}(T) = \sum_n \big(N_n(T)\big) \Big(\Omega_{PrNH_3(Solv)_n}(T) - \Omega_{PrNH_3}(T)\Big) \qquad \textit{Eq S5}$$

$$\Omega(T) = \Omega_{ion}(T) + \big(\Omega_{inc}(T)\big) \sum_i \left(\frac{SASA_i}{SASA_{free}}\right) \qquad \textit{Eq S6}$$

Using the modified Mason-Schamp equation, ion effective temperature can be estimated in a modified DMS environment using a self-consistent 2T theory approach described previously.[7,17] In this self-consistent method, $\Omega(T)$ and $m_{ion}(T)$, calculated using functional fits that describe its evolution as a function of T_{eff}, are used to evaluate ion mobility, and hence ion velocity ($v = \mathrm{KE}$) through equation 10. Since T_{eff} is not known, one can approximate by iteratively solving for ion velocity ($v = KE$) at $T = T_{bath}$ for a specific field strength. The ion velocity is calculated as the average over the course of a single duty cycle of the SV waveform. Given the maximum amplitude of the waveform (D) is two-thirds of peak-to-peak SV (SV_{pp}) voltage ($D = 2/3 \cdot SV_{pp}$), a gap height of 1 mm between the DMS electrodes (d), and oscillation frequency (ω) of 3 MHz, the field strength as function of time is defined by equation S7.

$$E(t) = \frac{D}{d}\left(\frac{2}{3}\sin(\omega t) + \frac{1}{3}\sin\left(2\omega t - \frac{\pi}{2}\right)\right) \qquad \textit{Eq S7}$$

The calculated ion velocity at $T = T_{bath}$ is then used to evaluate ion temperature using two-temperature theory (equation 9 in main text). Equation 9 is shown below for convenience. The new T_{eff} is then used to re-evaluate ion velocity, which is then used to again calculate T_{eff}. The process is completed iteratively until T_{eff} converges to a pre-defined threshold (here, $T_{eff} < 10^{-4}$ K).

$$T_{eff} = T_{bath} + T_{field} \approx T_{bath} + \frac{M}{3k_b}(KE)^2 \qquad \textit{Eq S8}$$

Molecular dynamics and CCS calculations of GGG, AAA, and Polybia-MP1

MD and SASA protocol:

For molecular dynamics calculations, Maestro (2020-3; Schrodinger, LLC) was employed. The starting peptide structures and their initial conformations were built in Maestro with the appropriate charge state for the N-terminus, C-terminus, and side chains. GGG, AAA, and MP1 were drawn in a helical starting conformation. All starting structures were then minimized using Macromodel and employed the OPLS3e forcefield* in vacuum. All minimizations were verified for convergence.

* "OPLS3e: Extending Force Field Coverage for Drug-Like Small Molecules" Roos, K.; Wu, C.; Damm, W.; Reboul, M.; Stevenson, J.M.; Lu, C.; Dahlgren, M.K.; Mondal, S.; Chen, W.; Wang, L.; Abel, R.; Friesner, R.A.; Harder, E.D., J. Chem. Theory Comput., 2019, 1863–1874,; Harder, E.; Damm, W.; Maple, J.; Wu, C.; Reboul, M.; Xiang, J.Y.; Wang, L.; Lupyan, D.; Dahlgren, M.K.; Knight, J.L.; Kaus, J.W.; Cerutti, D.; Krilov, G.; Jorgensen, W.L.; Abel, R.; and Friesner, R.A., "OPLS3: a force field providing broad coverage of drug-like small molecules and proteins," J. Chem. Theory Comput., 2016, 12, 281-296.

After the peptide starting structures were built and minimized as described above, the System Builder module (Schrodinger, LLC) was used to prepare the peptides for Molecular Dynamics runs. Settings were: Solvent model: None (for *in vacuo* MD runs) or full SPC water box (for full water solvation); Boundary Conditions: Box Shape: Cubic; Box size calculation method: Buffer; Distances: a = 10Å; b = 10Å, c = 10Å; force field: OPLS3e; Ion Placement: None. Following this step molecular dynamics simulations were run in Desmond. MD settings were: Simulation time: 200 ns; Recording interval: Trajectory: 200.0 ps; Energy 1.2; Approximate number of frames: 1000; Ensemble class: NVT; Temperature 500 K; Relax Model system before simulation: Yes; Integration (RESPA Integrator): Time step bonded: 2.0 fs near 2.00 far 6.00; Thermostat method: Nose-Hoover chain; Relaxation time: 1.0 ps; Coulombic Interactions: Short range method: cutoff radius of 9.0 A; No restraints used. Seed: custom 2007, randomize velocities. Forcefield OPLS3e. The exact sequence of

simulation stages were as follows: i) simulate Brownian dynamics NVT, T = 10 K, small timesteps and restraints on solute heavy atoms, 100 ps; ii) simulate, NVT, T = 10 K, small times steps, and restraints on solute heavy atoms, 12 ps; iii) simulate, NVT and no restraints.

Average Total energies (kcal/mol) for each MD run and their SDs were determined in Maestro using the Simulation Quality Analysis submodule. Block length for averaging was 10.0 ps. To determine the lowest energy conformation during the MD run, the Simulation Event Analysis submodule was employed to plot the energy for each conformation along the time coordinate. Lowest energy data points were then visually selected, and the associated conformation was isolated and exported for CCS calculations.

Solvent accessible surface areas (SASA) during the trajectory were computed and the average SASA and SD values were calculated after importing values from each snapshot into Excel. The atoms that were selected for the determination of their SASA were as follows:

N-terminus or Lys side chain: either NH_2 (neutral residues; 3 atoms) or NH_3^+ (protonated residues; 4 atoms).

Peptide charge states and results from MD simulation – [MP1 + 3H]$^{3+}$ and [MP1 + 2H]$^{2+}$ (*in vacuo*)

Table S2. The various protonation states of [MP1 + 3H]$^{3+}$ and [MP1 + 2H]$^{+}$, as well as the average energy of the system throughout the 200 ns MD simulation and the relative energies. The relative energies of the global minimum (GM) structure sampled throughout the MD run, as re-calculated at the ωB97X-D/6-31G(d) level of theory (Gibbs corrected) are also provided.

Peptide	**N-term (SASA / Å²)**	**Lys-4 (SASA / Å²)**	**Lys-5 (SASA / Å²)**	**Lys-11 (SASA / Å²)**	**MD Energy / kJ mol^{-1}**	**ωB97X-D/ 6-31G(d)**
[MP1 + 3H]$^{3+}$ (D)	0 (33.6 ± 9.8)	+ (5.7 ± 9.5)	+ (11.4 ± 11.1)	+ (8.3 ± 7.8)	576.3 ± 65.5	49.8
[MP1 + 3H]$^{3+}$ (E)	+ (11.1 ± 10.2)	0 (35.1 ± 11.3)	+ (7.5 ± 6.5)	+ (9.4 ± 8.3)	478.7 ± 69.0	39.2
[MP1 + 3H]$^{3+}$ (F)	+ (26.9 ± 17.8)	+ (2.7 ± 2.2)	0 (33.8 ± 11.8)	+ (5.7 ± 5.1)	472.2 ± 66.3	12.1
[MP1 + 3H]$^{+}$ (G)	+ (24.7 ± 22.3)	+ (3.7 ± 3.1)	+ (3.8 ± 3.7)	0 (32.6 ± 14.5)	510.6 ± 69.4	0.0
[MP1 + 2H]$^{3+}$ (H)	0 (25.1 ± 10.4)	0 (34.2 ± 18.9)	+ (3.9 ± 3.7)	+ (7.8 ± 7.2)	330.5 ± 59.8	118.2
[MP1 + 2H]$^{2+}$ (I)	0 (27.2 ± 9.8)	+ (3.5 ± 3.3)	0 (32.5 ± 17.6)	+ (3.3 ± 3.3)	338.7 ± 61.6	0.0
[MP1 + 2H]$^{2+}$ (J)	+ (5.0 ± 4.8)	0 (36.9 ± 13.9)	0 (28.7 ± 18.7)	+ (8.3 ± 7.7)	323.1 ± 59.9	114.8
[MP1 + 2H]$^{2+}$ (K)	+ (7.9 ± 7.8)	0 (36.6 ± 16.1)	+ (3.1 ± 3.1)	0 (35.5 ± 16.1)	313.5 ± 67.2	60.9
[MP1 + 2H]$^{2+}$ (L)	+ (5.2 ± 5.1)	+ (1.2 ± 1.2)	0 (43.8 ± 16.3)	0 (32.1 ± 18.1)	359.5 ± 62.2	92.6
[MP1 + 2H]$^{2+}$ (M)	0 (29.7 ± 10.1)	+ (2.2 ± 2.0)	+ (2.5 ± 2.3)	0 (38.7 ± 15.5)	358.2 ± 61.4	33.2

Peptide charge states and results from MD simulation – [GGG + H]$^+$ and [AAA + H]$^+$ (*in vacuo*)

Table S3. The solvent accessible surface area (SASA) of the [GGG + H]$^+$, [AAA + H]$^+$, and [$PrNH_3$]$^+$ systems throughout the 200 ns MD simulation and the relative energies.

Peptide	N-term SASA / Å^2
[GGG + H]$^+$	+ (53.7 ± 12.2)
[AAA + H]$^+$	+ (61.8 ± 6.4)
[$PrNH_3$]$^+$	+ (72.3 ± 3.8)

Peptide charge states and results from MD simulation – [MP1 + 3H]$^{3+}$ and [MP1 + 2H]$^{2+}$ (full water solvation)

Table S4. The various protonation states of [MP1 + 3H]$^{3+}$ and [MP1 + 2H]$^+$, as well as the average energy of the system throughout the 200 ns MD simulation and the relative energies using full water solvation.

Peptide	N-term (SASA / Å^2)	Lys-4 (SASA / Å^2)	Lys-5 (SASA / Å^2)	Lys-11 (SASA / Å^2)	MD Energy / kJ mol^{-1}
[MP1 + 3H]$^{3+}$ (D)	0	+	+	+	Not sampled
[MP1 + 3H]$^{3+}$ (E)	+ (51.5 ± 7.6)	0 (48.5 ± 14.7)	+ (67.0 ± 6.5)	+ (11.8 ± 8.3)	960.6 ± 25.1
[MP1 + 3H]$^{3+}$ (F)	+ (51.2 ± 7.8)	+ (68.4 ± 10.3)	0 (49.3 ± 14.4)	+ (67.9 ± 10.7)	957.1 ± 24.4
[MP1 + 3H]$^+$ (G)	+	+	+	0	Not sampled
[MP1 + 2H]$^{3+}$ (H)	0	0	+	+	Not sampled
[MP1 + 2H]$^{2+}$ (I)	0	+	0	+	Not sampled
[MP1 + 2H]$^{2+}$ (J)	+ (52.0 ± 7.0)	0 (49.7 ± 13.7)	0 (48.5 ± 14.6)	+ (66.9 ± 11.3)	972.2 ± 25.0
[MP1 + 2H]$^{2+}$ (K)	+ (50.8 ± 8.0)	0 (48.6 ± 15.1)	+ (67.7 ± 11.1)	0 (49.2 ± 14.8)	987.2 ± 25
[MP1 + 2H]$^{2+}$ (L)	+	+	0	0	Not sampled
[MP1 + 2H]$^{2+}$ (M)	0	+	+	0	Not sampled

Peptide charge states and results from MD simulation – $[GGG + H]^+$ and $[AAA + H]^+$ (full water solvation)

Table S5. The solvent accessible surface area (SASA) of the $[GGG + H]^+$, $[AAA + H]^+$, and $[PrNH_3]^+$ systems throughout the 200 ns MD simulation and the relative energies using full water solvation.

Peptide	N-term SASA / Å²
$[GGG + H]^+$	+ (72.8 ± 3.4)
$[AAA + H]^+$	+ (64.5 ± 2.6)
$[PrNH_3]^+$	+ (72.6 ± 3.8)

CCS calculations of peptides with MobCal-MPI

The structures of $[GGG + H]^+$, $[AAA + H]^+$, $[MP1 + 3H]^{3+}$, and $[MP1 + 2H]^{2+}$ and MobCal-MPI input and output files are provided in the accompanying .zip file.
Boltzmann-weighted CCSs are used for $[GGG + H]^+$ and $[AAA + H]^+$ at the respective temperature that the calculation is performed at. CCSs are calculated on geometries optimized at the B3LYP-D3/6-31++G(d,p) level of theory. Gibbs corrected energies are used in the Boltzmann-weighting scheme. Partial charges constrained to reproduce the molecular dipole moment are determined using the Merz-Singh-Kollman (MK) partition scheme and carried forward for CCS calculations using MobCal-MPI. All CCS calculations employed 10 complete cycles of mobility calculations, which use 48 points of velocity integration and 1024 points of impact parameter integration.

For $[MP1 + 3H]^{3+}$ and $[MP1 + 2H]^{2+}$, CCSs are calculated using the lowest energy structure obtained from all possible protonation states explored from MD simulations. The structures were optimized at the B3LYP-D3/6-31G(d) level of theory; Boltzmann-weighted CCSs are also used using Gibbs corrected energies. Partial charges constrained to reproduce the molecular dipole moment are determined using the Merz-Singh-Kollman (MK) partition scheme and carried forward for CCS calculations using MobCal-MPI. All CCS calculations employed 10 complete cycles of mobility calculations, which use 48 points of velocity integration and 1024 points of impact parameter integration.

Figure S3-21 and Table S3-6 summarize the fits of CCS to $CCS(T_{eff}) = a + b(T_{eff})^c$, where a, b, and c are fit parameters.

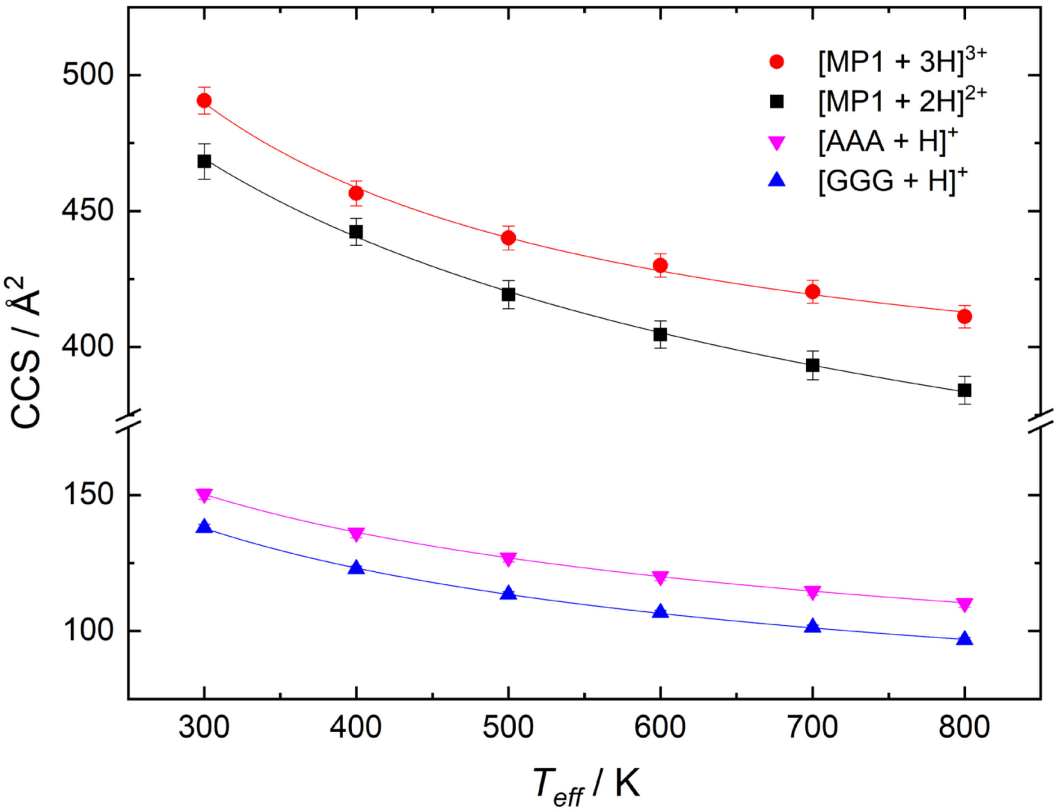

Figure S3-21. Fits of temperature-dependent CCS, as calculated by MobCal-MPI, to $CCS(T_{eff}) = a + b(T_{eff})^c$, where a, b, and c are fit parameters.

Table S3-6. Fit parameters (a, b, c) of temperature-dependent CCS, as calculated by MobCal-MPI, to $CCS(T_{eff}) = a + b(T_{eff})^c$.

Peptide	a	b	c
[MP1 + 3H]$^{3+}$	369.31 ± 17.41	44587.14 ± 55986.45	−1.03687 ± 0.2434
[MP1 + 2H]$^{2+}$	206.46 ± 82.8	2606.44 ± 1496.63	−0.402 ± 0.155
[AAA + H]$^{+}$	52.24 ± 6.06	2041.42 ± 373.297	−0.53228 ± 0.04264
[GGG + H]$^{+}$	47.761 ± 6.206	3038.4348 ± 798.8062	−0.6169 ± 0.0577

Functional fits describing mass and CCS increases of microsolvated clusters

Mass increases (m_{inc})

The mass increases (m_{inc}) defined by equation S3 in the supplementary information are shown in the figure below (scatter points) as a function of temperature (T) are fit to a biphasic sigmoid (equation S9) for ease of interpolation. Parameters of the biphasic sigmoid are shown in Table S3-7.

Biphasic sigmoid:

$$m_{inc} = A1 + (A2 - A1)\left[\frac{p}{1 + 10^{(b1-T)\bullet h1}} + \frac{1-p}{1 + 10^{(b2-T)\bullet h2}}\right] \qquad \textit{Eq S9}$$

Table S3-7. The parameters for the biphasic sigmoidal fit (A1, A2, p, b1, b2, h1, h2) as used in equation S3.

Solvent	A1	A2	b1	b2	h1	h2	p
H_2O	0.36016	139.092	385.2294	551.3023	-0.02951	-0.00396	0.36006
MeOH	-0.29071	263.2841	427.2449	616.5409	-0.01662	-0.00388	0.63839
EtOH	0.90336	368.6819	400.7997	696.701	-0.03619	-0.00775	0.72921
IPA	13.77176	421.1221	433.1637	731.0707	-0.05739	-0.00554	0.72958
ACE	3.06022	184.5	436.4612	785.1439	-0.01259	-0.0051	0.34115
MeCN	-9943.53	235.6167	398.4292	3178.461	-0.01706	-8.73E-04	0.00602

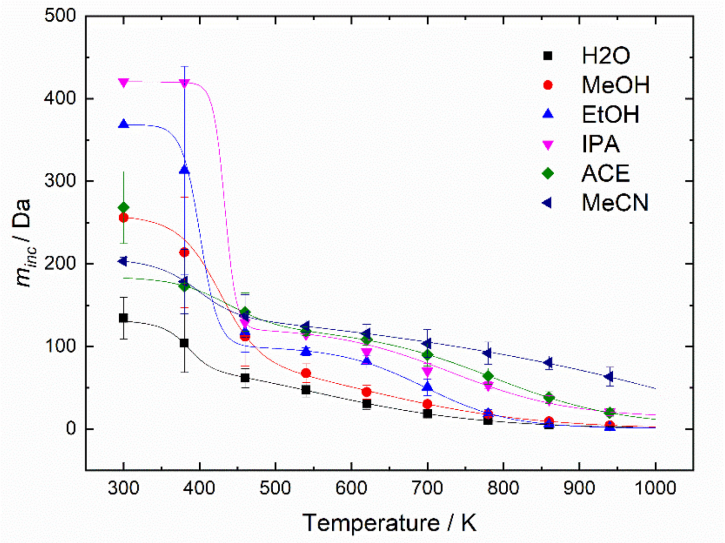

Figure S3-22. Functional fits of m_{inc} (Equation S3) to a biphasic sigmoidal function (Equation S7).

Collision cross section (CCS) calculations of microsolvated $[PrNH_3]^+$ species

The tables below describe the CCSs of $[PrNH_2 + H + n(Solv)]^+$, where n = 0 – 8 and Solv = H_2O, MeOH, EtOH, IPA, MeCN, and ACE. CCSs are calculated on the global minimum (Gibbs corrected) of the respective microsolvated cluster as determined at the MP2(full)/6-311++G(d,p)//ωB97X-D/6-311++G(d,p) level of theory. For IPA clusters, the MP2(full)/6-31+G(d,p)//ωB97X-D/6-31+G(d,p) level of theory is used. Partial charges constrained to reproduce the molecular dipole moment are determined using the Merz-Singh-Kollman (MK) partition scheme and carried forward for CCS calculations using MobCal-MPI. All CCS calculations employed 10 complete cycles of mobility calculations, which use 48 points of velocity integration and 1024 points of impact parameter integration.

Table S3-8. $[PrNH_2 + H + n(H_2O)]^+$ CCS calculations

Temp / K	n = 0	n = 1	n = 2	n = 3	n = 4	n = 5	n = 6	n = 7	n = 8	CCS_{inc} (H_2O)
300	116.42	116.28	119.36	124.83	132.97	140.53	150.13	159.66	165.47	45.84
400	99.18	99.74	103.75	109.85	117.79	125.42	135.22	144.17	149.46	25.11
500	87.35	88.79	93.55	99.92	107.90	115.43	125.16	134.14	139.07	13.29
600	78.71	81.04	86.19	92.89	101.12	108.45	118.01	126.93	131.69	7.73
700	72.14	75.22	80.84	87.71	96.01	103.30	112.66	121.46	126.16	3.74
800	67.03	70.69	76.71	83.72	92.02	99.25	108.51	117.28	121.82	1.88

Table S3-9. $[PrNH_2 + H + n(MeOH)]^+$ CCS calculations

Temp / K	n = 0	n = 1	n = 2	n = 3	n = 4	n = 5	n = 6	n = 7	n = 8	CCS_{inc} (MeOH)
300	116.42	118.94	128.33	140.79	155.73	166.60	176.59	183.83	201.58	85.04
400	99.18	102.98	113.20	125.70	140.52	151.04	160.61	167.86	185.43	60.76
500	87.35	92.72	103.43	115.93	130.66	140.89	150.32	157.49	174.79	23.94
600	78.71	85.43	96.62	109.01	123.69	133.63	143.03	150.20	167.26	13.02
700	72.14	79.95	91.52	103.91	118.51	128.27	137.60	144.62	161.62	7.83
800	67.03	75.75	87.59	99.95	114.43	124.10	133.37	140.29	157.04	4.30

Table S3-10. $[PrNH_2 + H + n(EtOH)]^+$ CCS calculations

Temp / K	n = 0	n = 1	n = 2	n = 3	n = 4	n = 5	n = 6	n = 7	n = 8	CCS_{inc} (EtOH)
300	116.42	125.63	140.45	157.75	175.99	187.02	193.68	201.08	219.09	102.66
400	99.18	109.71	125.12	142.54	160.58	171.18	178.85	185.39	202.66	59.60
500	87.35	99.32	115.16	132.60	150.27	160.56	168.97	174.91	191.89	31.02
600	78.71	91.97	108.18	125.60	143.17	153.04	161.93	167.37	184.24	27.29
700	72.14	86.50	102.99	120.38	137.84	147.45	156.76	161.76	178.49	16.58
800	67.03	82.23	98.97	116.31	133.62	143.14	152.64	157.35	173.97	4.62

Table S3-11. $[PrNH_2 + H + n(IPA)]^+$ CCS calculations

Temp / K	n = 0	n = 1	n = 2	n = 3	n = 4	n = 5	n = 6	n = 7	CCS_{inc} (IPA)
300	116.42	129.95	153.08	170.95	189.21	198.76	212.34	221.86	105.44
400	99.18	114.15	137.74	155.23	173.42	182.59	196.29	205.74	106.00
500	87.35	103.72	127.65	145.01	163.03	172.14	185.65	195.03	40.09
600	78.71	96.36	120.60	137.75	155.66	164.72	178.05	187.42	33.78
700	72.14	90.90	115.31	132.39	150.06	159.14	172.38	181.59	23.18
800	67.03	86.66	111.21	128.19	145.73	154.90	167.99	176.98	16.19

Table S3-12. $[PrNH_2 + H + n(MeCN)]^+$ CCS calculations

Temp / K	n = 0	n = 1	n = 2	n = 3	n = 4	n = 5	CCS_{inc} (MeCN)
300	116.42	122.30	138.88	159.04	189.34	207.19	89.92
400	99.18	106.48	124.13	143.73	172.63	189.81	69.84
500	87.35	95.97	114.46	133.70	161.79	178.40	50.12
600	78.71	88.59	107.74	126.68	154.03	170.09	46.03
700	72.14	83.18	102.69	121.43	148.23	163.95	40.46
800	67.03	78.98	98.79	117.27	143.65	159.12	34.98

Table S3-13. $[PrNH_2 + H + n(ACE)]^+$ CCS calculations

Temp / K	n = 0	n = 1	n = 2	n = 3	n = 4	n = 5	CCS_{inc} (ACE)
300	116.42	128.45	150.63	169.98	185.68	207.36	83.53
400	99.18	112.61	135.19	154.53	170.09	191.23	53.66
500	87.35	102.13	125.24	144.43	159.89	180.55	41.10
600	78.71	94.79	118.12	137.26	152.52	173.04	37.51
700	72.14	89.39	112.94	131.95	147.10	167.26	30.29
800	67.03	85.16	108.88	127.82	142.92	162.70	19.07

Collision cross section increases (CCS_{inc})

The increases in collision cross section defined by Equation S5 in the supplementary material are shown in Figure S23 (scatter points) as a function of temperature (T). CCS_{inc} are fit to a logistic function (Equation S10). The parameters for the logistic function (A_1, A_2, x_0, s) are shown in Table S14.

Logistic function:

$$CCS_{inc} = \frac{A_1 - A_2}{1 + \left(\frac{T}{x_0}\right)^s} + A_2 \qquad \textit{Eq S10}$$

Table S3-14. The parameters for the logistic fit (A1, A2, x_0, s) as used in equation S10.

Solvent	A_1	A_2	x_0	s
H_2O	95.39656	-2.23337	296.7593	3.15432
MeOH	110.6018	1.46958	392.1123	5.01033
EtOH	150.0005	-2.53294	384.2837	4.00051
IPA	129.0164	12.68171	424.2275	5.05474
ACE	5314.305	-78.9432	0.18253	0.47423
MeCN	187.5414	24.65389	253.1478	2.27641

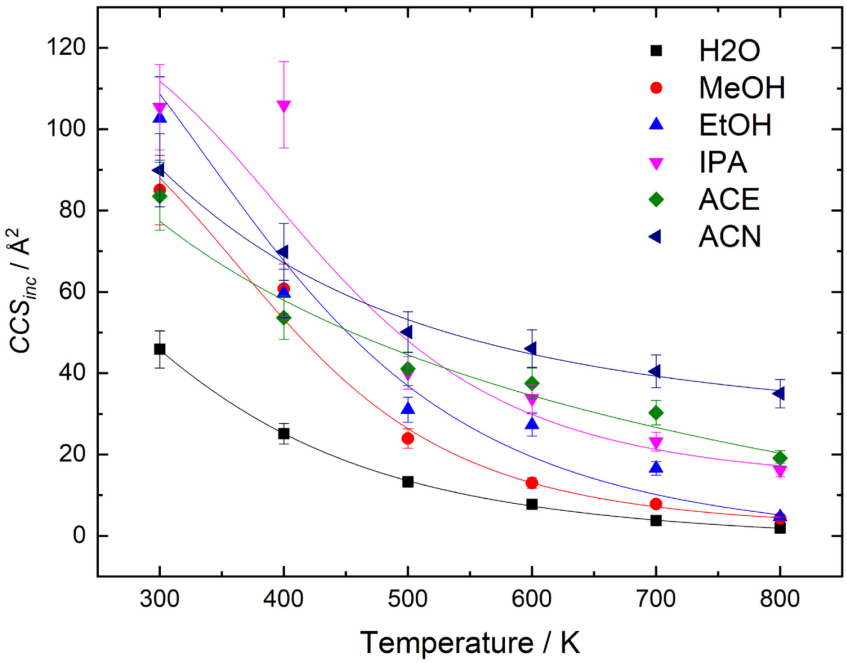

Figure S23. Functional fits of Ω_{inc} (Equation S5) to a logistic function (Equation S10).

Supplementary note: Frequently Asked Questions

If +4 states of MP1 are detected in environments seeded with acetone and acetonitrile, why is the max value of the Z-scale in Figure 3 3.0?

The intensities of the $[MP1 + 4H + n(Solv)]^{4+}$ adducts were three times lower than that of $[MP1 + 3H]^{3+}$ and roughly equivalent to the intensity of $[MP1 + 2H]^{2+}$. As such, the z-scale of the contour map in Figure 7 was fixed between 2 and 3 to illustrate the changes in population-weighted charge, which reached a maximum of 3.16 in the presence of aprotic modifiers.

The DMS experiments here use repeating evaporation/condensation cycles driven by the oscillating SV. During each of these cycles, shouldn't the heat production associated with condensation match the cooling associated with evaporation? (conservation of energy).

The oscillating waveform generates a dynamic condensation/evaporation cycle. However, since the ion-solvent cluster is not embedded in a closed system, the same molecules of N_2, solvent modifier, and analyte do not interact with each collision. Cluster formation/dissociation in the DMS occurs in an open system, as analyte motion is driven by the transverse oscillating electric field and the axial gas flow established by the pressure differential between the DMS cell and mass spectrometer. Assuming ergodicity, internal energy resulting from collision with background gas will sample all internal degrees of freedom of the $[M+(solv)_n]^+$ cluster. Once that energy surpasses the lowest thermodynamic threshold for dissociation (loss of a solvent molecule). That threshold will be accessed irreversibly yielding $[M+(solv)_{n-1}]^+$ species with low internal energy. This is the basis for how the evaporative cooling mechanism operates.

Regarding the point of heat production associated with condensation matching the cooling associated with evaporation, the ion's velocity, and hence it's internal energy, must be considered. Even though the integral over the course of a single duty cycle is zero, DMS operates by harnessing the differential mobility incurred by an ion under high- and low-field conditions. Since all points in the duty cycle of the DMS waveform exceed the low-field limit, the inequality $v \leq KE$ holds and becomes more pronounced as field-strength increases. Thus, the velocity of the ion (and hence, its internal energy) lags behind instantaneous changes in field strength. So, the heating imparted to an ion during the high field portion is not equivalent to that of the low-field portion. Moreover, since the ion's effective temperature during the low and high field portions are different, the number of solvent molecules non-covalently bound will also be different. This translates to a differing ion mobility K, and consequently a differing ion velocity and internal energy distribution. Since the microsolvation state of an analyte is different under high-field and low-field conditions, the heat production associated with condensation will not match the cooling associated with evaporation.

References

(1) de Grotthuss, C. J. T. Sur La Décomposition de l'eau et Des Corps Qu'elle Tient En Dissolution à l'aide de l'électricité Galvanique. *Ann. Chim.* **1806**, *LVIII*, 54–74.

(2) Malloum, A.; Fifen, J. J.; Conradie, J. Solvation Energies of the Proton in Methanol Revisited and Temperature Effects. *Phys. Chem. Chem. Phys.* **2018**, *20* (46), 29184–29206.

(3) Malloum, A.; Malloum, A.; Fifen, J. J.; Conradie, J. Exploration of the Potential Energy Surfaces of Small Ethanol Clusters. *Phys. Chem. Chem. Phys.* **2020**, *22* (23), 13201–13213.

(4) Knochenmuss, R.; Cheshnovsky, O.; Leutwyler, S. Proton Transfer Reactions in Neutral Gas-Phase Clusters: 1-Naphthol with H2O, D2O, CH3OH, NH3 and Piperidine. *Chem. Phys. Lett.* **1988**, *144* (4), 317–323.

(5) Boyd, S. L.; Boyd, R. J. A Density Functional Study of Methanol Clusters. *J. Chem. Theory Comput.* **2007**, *3* (1), 54–61.

(6) Haack, A.; Polaczek, C.; Tsolakis, M.; Thinius, M.; Kersten, H.; Benter, T. Charge Retention/Charge Depletion in ESI-MS: Theoretical Rationale. *J. theAmerican Soc. Mass Spectrom.* **2020**, *31*, 785–795.

(7) Haack, A.; Crouse, J.; Schlüter, F.-J.; Benter, T.; Hopkins, W. S. A First Principles Model of Differential Ion Mobility: The Effect of Ion-Solvent Clustering. *J. Am. Soc. Mass Spectrom.* **2019**, *30 (12),* 2711-2725 .

(8) Krylov, E. V.; Nazarov, E. G. Electric Field Dependence of the Ion Mobility. *Int. J. Mass Spectrom.* **2009**, *285* (3), 149–156.

(9) Thinius, M.; Polaczek, C.; Langner, M.; Bräkling, S.; Haack, A.; Kersten, H.; Benter, T. Charge Retention/Charge Depletion in ESI-MS: Experimental Evidence. *J. Am. Soc. Mass Spectrom.* **2020**, *31* (4), 773–784.

(10) Jordan, M. J. T.; Del Bene, J. E. Unraveling Environmental Effects on Hydrogen-Bonded Complexes: Matrix Effects on the Structures and Proton-Stretching Frequencies of Hydrogen-Halide Complexes with Ammonia and Trimethylamine. *J. Am. Chem. Soc.* **2000**, *122* (9), 2101–2115.

(11) Bende, A.; Muntean, C. M. The Influence of Anharmonic and Solvent Effects on the Theoretical Vibrational Spectra of the Guanine-Cytosine Base Pairs in Watson-Crick and Hoogsteen Configurations. *J. Mol. Model.* **2014**, *20* (3), 1–12.

(12) Ieritano, C.; Featherstone, J.; Carr, P. J. J.; Marta, R. A.; Loire, E.; McMahon, T. B.; Hopkins, W. S. The Structures and Properties of Anionic Tryptophan Complexes. *Phys. Chem. Chem. Phys.* **2018**, *20* (41), 26532–26541.

(13) Ieritano, C.; Crouse, J.; Campbell, J. L.; Hopkins, W. S. A Parallelized Molecular Collision Cross Section Package with Optimized Accuracy and Efficiency. *Analyst* **2019**, *144* (5), 1660–1670.

(14) Chai, J.; Head-Gordon, M. Long-Range Corrected Hybrid Density Functionals with Improved Dispersion Corrections. *Phys. Chem. Chem. Phys.* **2008**, *10* (44), 6615–6620.

(15) Singh, U. C.; Kollman, P. A. An Approach to Computing Electrostatic Charges for Molecules. *J. Comput. Chem.* **1984**, *5* (2), 129–145.

(16) Besler, B. H.; Merz, K. M.; Kollman, P. A. Atomic Charges Derived from Semiempirical Methods. *J. Comput. Chem.* **1990**, *11* (4), 431–439.

(17) Ieritano, C.; Featherstone, J.; Haack, A.; Guna, M.; Campbell, J. L.; Hopkins, W. S. How Hot Are Your Ions in Differential Mobility Spectrometry? *J. Am. Soc. Mass Spectrom.* **2020**, *31* (3), 582–593.